University of Alberta

Tailoring the Surface Chemistry of Germanium Quantum Dots

by

Enrico Wing Kei Fok

A thesis submitted to the Faculty of Graduate Studies and Research
in partial fulfillment of the requirements for the degree of

Master of Science

Department of Chemistry

Edmonton, Alberta
Spring 2008

Library and Archives Canada

Published Heritage Branch

395 Wellington Street
Ottawa ON K1A 0N4
Canada

Bibliothèque et Archives Canada

Direction du Patrimoine de l'édition

395, rue Wellington
Ottawa ON K1A 0N4
Canada

Your file Votre référence
ISBN: 978-0-494-45809-9
Our file Notre référence
ISBN: 978-0-494-45809-9

NOTICE:
The author has granted a non-exclusive license allowing Library and Archives Canada to reproduce, publish, archive, preserve, conserve, communicate to the public by telecommunication or on the Internet, loan, distribute and sell theses worldwide, for commercial or non-commercial purposes, in microform, paper, electronic and/or any other formats.

The author retains copyright ownership and moral rights in this thesis. Neither the thesis nor substantial extracts from it may be printed or otherwise reproduced without the author's permission.

AVIS:
L'auteur a accordé une licence non exclusive permettant à la Bibliothèque et Archives Canada de reproduire, publier, archiver, sauvegarder, conserver, transmettre au public par télécommunication ou par l'Internet, prêter, distribuer et vendre des thèses partout dans le monde, à des fins commerciales ou autres, sur support microforme, papier, électronique et/ou autres formats.

L'auteur conserve la propriété du droit d'auteur et des droits moraux qui protège cette thèse. Ni la thèse ni des extraits substantiels de celle-ci ne doivent être imprimés ou autrement reproduits sans son autorisation.

In compliance with the Canadian Privacy Act some supporting forms may have been removed from this thesis.

While these forms may be included in the document page count, their removal does not represent any loss of content from the thesis.

Conformément à la loi canadienne sur la protection de la vie privée, quelques formulaires secondaires ont été enlevés de cette thèse.

Bien que ces formulaires aient inclus dans la pagination, il n'y aura aucun contenu manquant.

Canada

Abstract

Semiconductor Quantum Dots (QDs) exhibit size-dependent optical, electronic, and chemical properties that arise from quantum confinement. As a result of these unique characteristics, QDs have many potential applications including biological labels, light emitting diodes, solar cells, liquid crystals, and transistors. The introduction of the following thesis outlines how and why these properties arise from the electronic structure of semiconductors. The most widely studied semiconductor material is CdSe and is known to be toxic and electrochemically unstable. Germanium, an elemental semiconductor is an attractive material because of its semiconductor properties, electrochemical stability, and large exciton radius. The present thesis outlines the synthesis of solution-borne hydride surface terminated Ge nanoparticles of varied diameters and crystallinity via room and elevated (*i.e.*, 300°C) temperature metal hydride reduction GeX_4 (X = Cl, Br, or I) using $LiAlH_4$. Subsequent thermal or photochemical initiated hydrogermylation of terminal alkenes (*e.g.*, C_nH_{2n} n = 5, 10 - 12) yielded solution processable, air stable *n*-alkyl terminated Ge nanoparticles. The Ge nanoparticles exhibit absorption maxima that can be assigned to the direct $\Gamma_{25} - \Gamma_{15}$ transitions at X (4.3 eV) and at Γ (3.4 eV) in bulk germanium. Particles were characterized using FT-IR and ^{1}H NMR spectroscopies, selected area electron diffraction, transmission electron microscopy, energy dispersive x-ray analysis, and X-ray powder diffraction. Experiments in this thesis outline the first surface functionalization of Ge nanoparticles via hydrogermylation.

Acknowledgements

I wish to recognize the efforts and support of the many individuals who have helped me become the person I am today. I am grateful to them for helping me achieve my goals. Identifying all those who have changed my life through these years is difficult; to those of you who have been inadvertently missed, thank you for being there.

A special thanks to those listed below:

- Professor Jonathan G. C. Veinot (Supervisor) for his advice, encouragement, patience, and support.
- Dr. Bryan Rowsell (Postdoctoral Fellow) and Dr. Al Meldrum for their collaboration and advice.
- Eric Henderson, Colin Hessel, Janet Macdonald, Shaune McFarlane, De-ann Rollings, and José Rodriguez (graduate colleges) for their friendship, as well as the countless hours they spent helping me prepare for my defense.
- Kristy Boates, Leah Coumont, Joel Kelly, Michelle Lockyer, Davin Piercey, Meiling Shih, and Victoria Russell (undergraduates) for their collaboration with me on various projects and for providing food during group meetings.
- Staff in the Department of Chemistry at the University of Alberta for their assistance and friendly advice.
- The U of A, Canada Foundation for Innovation (CFI), Alberta Science and Research Investments Program (ASRIP), and Natural Sciences and Engineering Research Council (NSERC) for financial support.
- Mom and Dad for their love, patience, understanding, and endless support.

- Members of the B^2 cell group, Chinese Anglican Parish of Holy Trinity, Edmonton Chinese Christian Church, Edmonton Chinese Baptist Church Love Fellowship, for their prayer support, laughter, and tears.
- Jacky Chan for her love and for being there for me when I needed her.
- Jacky's mom and dad for support and encouragement, and for helping me maintain a proper diet while I prepared for my defense.
- Jesus Christ for everything.

Table of Contents

1. Introduction 1

1.1. Semiconductors 1

1.1.1. What Is a Semiconductor? 1

1.1.2. Band Theory 1

1.1.2.1. Formation of Bands 2

1.1.2.2. Band Structure of Semiconductors 3

1.1.2.3. Occupation of Orbitals and Electrical Conductivity 4

1.1.3. Classification of Semiconductors 6

1.1.3.1. Compound vs. Elemental 6

1.1.3.2. Indirect vs. Direct Band Gap 7

1.2. From Atoms to Structures 8

1.2.1. Quantum Confinement 8

1.2.2. 0-D, 1-D, 2-D Semiconductor Structures 10

1.3. Current Semiconductor Nanocrystal Research 11

1.3.1. CdS and CdSe Nanoparticles 11

1.3.1.1. Size-Dependent Properties 12

1.3.1.2. Possible Shapes of CdSe Nanoparticles 13

1.3.1.3. Surface Chemistry 16

1.3.1.4. Multiple Core Shell Nanoparticles 17

1.4. Synthesis of Surface-Functionalized Group IV Semiconductor Nanoparticles 22

1.4.1. Particle Synthesis 23

1.4.2. Surface Functionalization 23

1.4.3. Synthesis of Germanium Nanoparticles 24

1.4.4. Synthesis of Silicon Nanoparticles 29

1.5. Nanoscience and Nanotechnology 33

1.5.1. What Is *Nano*? 33

1.5.2. What Is Nanotechnology? 33

1.5.3. Nano in History 33

1.5.4. Nano in Science 35

1.5.4.1. Carbon Nanotubes 35

1.5.4.2. Porous Silicon 35

1.5.4.3. Other Elemental Nanoparticles and Their Applications. . . . 36

1.6. Our Goals 36

2. Metal Hydride Reduction of GeX_4 Nanoparticles 39

2.1. Introduction 39

2.2. Experimental 41

2.2.1. Solvents and Reagents 41

2.2.2. Material Characterization 42

2.2.2.1. Spectroscopic Characterization 42

2.2.2.2. Electron Microscopy 42

2.2.3. Synthesis of Hydride Surface-Terminated Ge Nanoparticles 43

2.2.4. Extraction of Alkyl Surface-Terminated Ge Nanoparticles from **(1)** via Hydrogermylation 43

2.3. Results and Discussion 45

2.3.1. Fourier Transform Infrared Spectroscopy 45

2.3.2. ^{1}H Nuclear Magnetic Resonance Spectroscopy 47

2.3.3. Transmission Electron Microscopy 50

2.3.4. Selected Area Electron Diffraction 53

2.3.5. Ultraviolet Visible Spectroscopy 54

2.4. Conclusion 56

3. High Temperature Reduction of GeX_4 58

3.1. Introduction 58

3.2. Experimental 59

3.2.1. Reagents 59

3.2.2. Material Characterization 60

3.2.2.1. Spectroscopy Characterization 60

3.2.2.2. Electron Microscopy 60

3.2.3. Synthesis of Hydride Surface-Terminated Ge Nanoparticles 61

3.2.4. *n*-alkyl Surface Termination of **5a**, **5b**, and **5c** 61

3.3. Results and Discussion 62

3.3.1. Transmission Electron Microscopy 62

3.3.2. Energy-Dispersive X-Ray Spectroscopy 64

3.3.3. X-ray Powder Diffraction 65

3.3.4. Fourier Transform Infrared Spectroscopy 70

3.3.5. ^{1}H Nuclear Magnetic Resonance Spectroscopy 72

3.4. Conclusion 74

4. Conclusion and Future Work 76

5. References 79

List of Tables

Table 1 FT-IR data for hydride-terminated Ge nanoparticles samples. 46

Table 2 FT-IR data for alkyl-terminated Ge nanoparticles samples 47

Table 3 ^{1}H NMR data for alkyl-terminated Ge nanoparticles samples 50

Table 4 Optical absorption wavelength of different Ge nanoparticle samples 56

Table 5 TEM data for Ge nanoparticles samples 64

Table 6 EDX data for Ge nanoparticles samples 65

Table 7 XRD data for Ge nanoparticles analyzed prior to hydrogermylation 67

Table 8 Scherrer analysis of all reflections from XRD of **5a** 69

Table 9 FT-IR data for hydride- and pentane-terminated Ge nanoparticles 72

Table 10 ^{1}H NMR data for alkyl-terminated Ge nanoparticles samples 74

List of Figures

Figure 1 Formation of bands from multiple atoms that are brought into the bonding assembly. As the number (*N*) of atoms bonded together approaches infinity, a pseudo-band consisting of *N* different molecular orbitals of similar energy are formed 3

Figure 2 Band structure of a semiconductor and an insulator 4

Figure 3 At T = 0 K, only the valence band is filled with electrons. At T > 0 K, conduction occurs when electrons excited by thermal or photon energy are raised across the energy gap (Eg) forming charge carriers.. The positive carrier is the electron hole in the valence band; the negative carrier is the electron in the conduction band. Luminescence occurs when an energized electron in the conduction band returns to the hole in the valence band. A photon of light may be released when the electron drops across the energy gap 6

Figure 4 Arrows show examples of direct band gap (left) and indirect band gap (right) energy transitions. Left: Band diagram of a direct gap semiconductor: gallium arsenide. The direct band gap ($\Gamma \rightarrow \Gamma$) absorption is present in the Γ orientation of the crystal lattice.[10] Right: Band diagram of an indirect band gap semiconductor: bulk germanium. The indirect band gap ($\Gamma \rightarrow L$) absorption is present 7

Figure 5 Difference of band patterns between bulk semiconductors, nanocrystal semiconductors, and atom 9

Figure 6 Size-dependent emission of (HDA)-TOPO-TOP (hexadecylaminetrioctyl-phosphine oxide-trioctylphosphosine) capped CdSe/ZnS nanoparticles. Depending on their size, nanoparticles can emit in the whole visible spectra region with a quantum efficiency of 40 to 70% 10

Figure 7 Semiconductor quantum structures 11

Figure 8 Optical absorption spectra of CdSe nanoparticles in many different sizes. The nanoparticles were dispersed in hexane, and the collection of data was done at room temperature 13

Figure 9 Transmission electron micrographs of CdSe nanorods in (a) short (5.0 × 18.0 nm) and (b) long (4.5 × 36.0 nm) sizes 14

Figure 10 Transmission electron micrographs of CdSe teardrop-shaped nanoparticles 15

Figure 11 Transmission electron micrographs of CdSe teardrop-shaped nanoparticles 15

Figure 12 Transmission electron micrographs of self-assembled CdSe nanorods in (a) tracks and (b) superstructures. The insert in (b) shows the antiparallel dipole pairing of the CdSe nanorods, which is the preferred orientation 15

Figure 13 Transmission electron micrographs of TDPA-HDA-TOPO-TOP-capped CdSe nanoparticles synthesized following Scheme 3 17

Figure 14 Absorption spectra for one- or two-monolayer ZnS-coated CdSe nanoparticles (solid lines) and bare CdSe nanoparticles (dashed lines). CdSe nanoparticles have diameters measuring (a) 2.3 nm, (b) 4.2 nm, (c) 4.8 nm, and (d) 5.5 nm 19

Figure 15 Transmission electron micrographs of (a) CdSe, (b) CdSe/ZnSe, (c) CdSe/ZnSe/ZnS nanoparticles grown following Scheme 5 20

Figure 16 Absorption spectra for (a) CdSe nanoparticles, (b) CdSe/ZnSe (core/shell) nanoparticles (ZnSe ~ 2 monolayers of thickness), (c) CdSe/ZnSe/ZnS (core/shell/shell) nanoparticles (ZnS ~ 2 monolayers of thickness), and (d) CdSe/ZnSe/ZnS (core/shell/shell) nanoparticles (ZnS ~ 4 monolayers of thickness) 21

Figure 17 Effect that shell thickness has on PL quantum efficiency on various monolayers of multiple-shell CdSe nanoparticles 22

Figure 18 Chemical structure of CTAB 40

Figure 19 Chemical structure of Triton X-100 (n = 50 - 100) 40

Figure 20 FT-IR of crude reaction mixture of (**2**) showing ν_{Ge-H} stretching at 2067 cm^{-1} 45

Figure 21 IR spectra of Ge-QD synthesized using $GeCl_4$ and functionalized with 1-pentene (**4a**) and 1-dodecene (**4b**) by photochemical-initiated hydrogermylation 47

Figure 22 ^1H NMR spectra of Ge nanoparticle that had undergone hydrogermylation with 1-dodecene (**3c**) 49

Figure 23 Transmission electron micrographs of ~ 3 nm Ge-QD (**3d**). The bar on the Transmission electron micrographs represents 20 nm 51

Figure 24 Transmission electron micrographs of Ge nanoparticles synthesized using GeI_4 and terminated with undecane (**3b**). The size of the nanoparticles

averaged 5 nm and ranged from 2 to 10 nm. The bar on each Transmission electron micrographs represents 100 nm 52

Figure 25 The sizes of Ge nanoparticles synthesized using GeI_4 and terminated with undecane (**3b**) were determined by measuring a total of 408 particles from different regions of the TEM grid. The average diameter of the nanoparticles was 5 nm with a range from 2 to 10 nm 53

Figure 26 Selected electron diffraction of Ge nanoparticles synthesized using GeI_4 and terminated with undecane (**3b**). The pattern is indexed as (111), (220), (311), (331), and (440) lattice spacing of Ge 54

Figure 27 UV visible spectra of Ge-QD synthesized using GeI_4 56

Figure 28 The structure of TOP, colorless liquid surfactant 58

Figure 29 Transmission electron micrographs of Ge nanoparticles (black dots) synthesized using GeI_4 with an average particle size of 5.8 nm (n = 78). . .63

Figure 30 EDX analysis of Ge nanoparticles synthesized using GeI_4 indicates the presence of multiple elements 63

Figure 31 XRD of the black powder product collected before hydrogermylation (**5a**, **5b**, and **5c**). The surface of the Ge nanoparticle is hydride terminated. The peaks with grey arrows correspond to the peaks found in Ge powder. The peak highlighted with a black arrow is from an uncharacterized impurity. The peaks marked "X" are peaks from the Al sample holder 67

Figure 32 XRD of the black powder product collected after being terminated with pentane (6a, 6b, and 6c). The peaks marked "X" are peaks from the Al sample holder 68

Figure 33 Scherrer equation was used to estimate the diameter (D) of the Ge nanoparticles. K is the shape factor which has a value of 0.9. λ is the wavelength of the x-ray radiation (1.54056Å). B_p is the broadening of the peak at full width at half maximum (FWHM) (in radians). θ_B is the Bragg angle at half width 69

Figure 34 IR spectra of the brown products collected prior to and after hydrogermylation of Ge nanoparticles with 1-pentene 71

Figure 35 ^{1}H NMR spectra of the brown product synthesized using $GeCl_4$ (**6a**). This ^{1}H NMR sample was prepared using $CDCl_3$ 74

List of Schemes

Scheme 1 Method to synthesize CdSe nanoparticles employed by Murray *et al.* TOP/TOPO-capped CdSe can be synthesized by the decomposition of dimethylcadmium (Me_2Cd) and trioctylphosphine selenide (TOPSe) in the presence of a coordinating solvent trioctylphosphine (TOP) and trioctylphosphine oxide (TOPO) and heated to ~ 300°C under 1 atm of argon 12

Scheme 2 Method to synthesize CdSe nanoparticles employed by Manna *et al.* The selenium powder and dimethylcadium precursors were dissolved in tri-*n*-butylphosphine (TBP) and injected into a mixture of hexylphosphonic acid (HPA), tetradecylphosphonic acid (TDPA), and trioctylphosphine oxide (TOPO). The mixture was heated to 360°C, and a mixture of dimethylcadmium dissolved in TBP was added 14

Scheme 3 A method of preparing (HDA)-TOPO-TOP-capped CdSe nanoparticles employed by Rogach *et al.* The hexadecylamide tri-*n*-octylphosphine oxide-tri-*n*-octylphosphine (HDA-TOPO-TOP) capped CdSe nanoparticle is synthesized by dissolving TOPSe and Me_2Cd into TOP, then adding TOPO and HDA. The mixture is then heated to 300°C to promote crystal growth. The addition of an acidic component, *n*-tetradecyl phosphonic acid (TDPA), can further minimize the size distribution 16

Scheme 4 Synthesis of (CdSe)ZnS nanoparticles employed by Dabbousi *et al.* The CdSe nanoparticles passivated with TOPO are mixed with diethylzinc

($ZnEt_2$) and hexamethyldisilathiane $(TMS)_2S$ at the desired temperature to form a ZnS-overcoated CdSe quantum dot 18

Scheme 5 Synthetic pathways of CdSe/ZnSe/ZnS nanoparticles employed by Talapin *et al.* CdSe/ZnSe nanoparticles are prepared by adding HDA-TOPO-TOP-capped CdSe to a ZnSe solution made using $Zn(C_2H_5)_2$ and TOPSe. The stock solution of ZnS is prepared by mixing $Zn(C_2H_5)_2$ with $(CH_3)_3SiSSi(CH_3)_3$ (bis[trimethylsilyl]sulphide) and adding this mixture to a solution of CdSe/ZnSe at 200 to 220°C 20

Scheme 6 Germanium tetrachloride reduced in solution with lithium naphthalene, yielding germanium nanoparticles. An organic methyl group (Me_3SiCl) is used to terminate dangling bonds on the surface of the germanium nanoparticle 25

Scheme 7 Method to synthesize germanium particles employed by Heath *et al.* In this reaction, M represents either Ge or Si; R represents any organic functional group. The R group acts as a capping agent to limit the size of the nanoparticles synthesized and to keep the nanoparticles separated. NaK alloy dispersion (in heptane) is used as the reduction agent. Ge_{diam} represents the diameter of Ge 26

Scheme 8 Germanium nanoparticle synthesis from the reaction of Zintl salt and Mg_2Ge with $GeCl_4$ in the presence of 2-methoxy ethyl ether. The product, Q-Ge-Cl, is Cl-terminated Ge nanoclusters 26

Scheme 9 Method of germanium nanoparticle (Q-Ge) synthesis described by Wilcoxon *et al.* The X in the reaction represents halogens, including chloride, bromide, and iodide 27

Scheme 10 & Scheme 11 Method in preparing germanium nanoparticles described by Lu *et al.* The size of the nanoparticles can be controlled by the concentration of GeI_2 dissolved in the surfactant tri-*n*-octylphosphine (TOP) and tri-*n*-butylphosphine (TBP) 28

Scheme 12 Thermolysis of Ge precursor, $Ge[N(SiMe_3)_2]_2$, described by Gerung *et al* 29

Scheme 13 Solution-based synthesis of silicon nanoparticles described by Bley *et al.* This solution reaction is carried out by refluxing a solution of KSi with excess $SiCl_4$ in the glyme, diglyme, or THF 30

Scheme 14 The surface of the silicon nanoparticle, presumed to be chlorine terminated, was chemically modified by exposure to methanol at room temperature. . 30

Scheme 15 Solution methods commonly used to tailor the surface of silicon nanoparticles 31

Scheme 16 Reduction of $SiCl_4$ with sodium naphthalide and glyme gives chlorine terminated silicon nanoparticles. Excess n-octanolis added to change the silicon surface termination from Cl to octanol 31

Scheme 17 The oxide layer on an oxide-coated silicon nanoparticle can be removed by etching it away with hydrofluoric acid and nitric acid, thereby forming hydride-terminated silicon nanoparticles. Hydrosilylation can be initiated photochemically in the presence of a terminal alkene 32

Scheme 18 Reduction of $SiCl_4$ with $LiAlH_4$ which forms a hydrogen- terminated silicon nanoparticle stabilized by tetraoctylammonium bromide (TOAB). Hexachloroplatinic acid (Pt catalyst) and the terminal alkene (*e.g.*, 1-heptene) are added to change the surface of the silicon nanoparticle 32

Scheme 19 General scheme that can be used to make germanium nanoparticles from GeX_4 (X = Cl and I). Metal hydride reduction of $GeBr_4$ was not investigated and will not be discussed in this chapter. Surfactants used to limit particle growth included cetyltrimethylammonium bromide (CTAB) and Triton X-100. The unidentified products are the uncharacterized yellow salts present in the solution 40

Scheme 20 Reaction scheme for hydrogermylation of Ge nanoparticles. Hydride surface-terminated germanium nanoparticles were heated or exposed to a constant white light source in the presence of excess terminal alkenes, which yielded an alkyl surface-terminated Ge-QD 40

Scheme 21 High temperature reduction of GeX_4 to yield Ge nanoparticles. $LiAlH_4$ is added to a 300°C mixture of germanium precursor GeX_4 (X = Cl, Br, or I) dissolved in trioctylphosphine (TOP) (see Figure 28) 56

Scheme 22 The reaction scheme for hydrogermylation of Ge-NP. Hydrogen surface-terminated germanium nanoparticles from Scheme 21 are heated with excess terminal alkenes. 1-pentene was routinely used to terminate the surface of Ge-QD 57

List of Abbreviations

CB	conduction band
CNT	carbon nanotube
CTAB	Cetyltrimethylammonium bromide
DC	direct current
EDS or EDX	energy-dispersive X-ray spectroscopy
EELS	electron energy loss spectroscopy
E_g	band gap
FT-IR	Fourier transform infrared spectroscopy
FWHM	full width at half maximum
HAD	hexadecylamine
HDA	hexadecylamide
HOMO	highest occupied molecular orbital
HPA	hexylphosphonic acid
HPLC	high performance liquid chromatography
HRTEM	high resolution transmission electron microscopy
LUMO	lowest unoccupied molecular orbital
MO	molecular orbital
NMR	nuclear magnetic resonance spectroscopy
PL	photoluminescence spectroscopy
PS	porous silicon
QD	quantum dot
QW	quantum well

QWR	quantum wire
SAED	selected area electron diffraction
SEC	size exclusion chromatography
TBP	tri-*n*-butylphosphine
TDPA	tetradecylphosphonic acid
TEM	transmission electron micrograph
THF	tetrahydrofuran
TMS	tetramethyl silane
TOAB	tetraoctylammonium bromide
TOP	trioctylphosphine
TOPO	trioctylphosphine oxide
UV	ultraviolet visible spectroscopy
VB	valence band
XRD	x-ray powder diffraction

1. Introduction

1.1. Semiconductors

The following section outlines some basic properties of semiconductors. Elementary band theory will be used to assist with understanding the electronic properties of the semiconductor.

1.1.1. What Is a Semiconductor?

A semiconductor is a material that exhibits electrical conductivity intermediate between metals and insulators.[1,2] While one might expect that the term *semiconductor* refers to a material that can behave both as an insulator and a conductor, this class of material has distinctively different electronic characteristics. One difference is in the way the electrical conductivity of semiconductors and metals responds to heating. Another difference is how changes in the purity of a semiconductor can affect its electrical conductivity. A basic understanding of band theory is necessary to understand the electronic structure of semiconductors and how conductivity can be tailored.

1.1.2. Band Theory

Band theory, an extension of molecular orbital theory, is commonly used to explain the electronic structure of materials such as semiconductors.[2,3] To begin the discussion on band theory, it is important to understand how energy bands are formed by orbitals.

1.1.2.1.Formation of Bands

Each atom within a solid network has its own set of corresponding atomic orbitals. The formation of bands from atomic orbitals begins with the bonding of two atoms. Any two identical, isolated atoms will have atomic orbitals with the same energy. When these atoms are brought into a bonding configuration, two atomic orbitals interact and split into two new molecular orbitals (MOs) with different energies (bonding and antibonding). If a third atom is brought into the bonding assembly, the "new" atomic orbital will interact with the other two atomic orbitals, forming three molecular orbitals. As the number of atoms bonded becomes increasingly large, the energy difference between levels becomes infinitesimally small, giving rise to a pseudo-continuous band of "molecular" orbitals. If the atoms have *s* orbitals, the band formed by the overlap of *s* orbitals is called the *s* band. Similarly, a band formed by the overlap of *p* orbitals is called the *p* band. A pictorial presentation of how bands are formed is found in Figure 1.

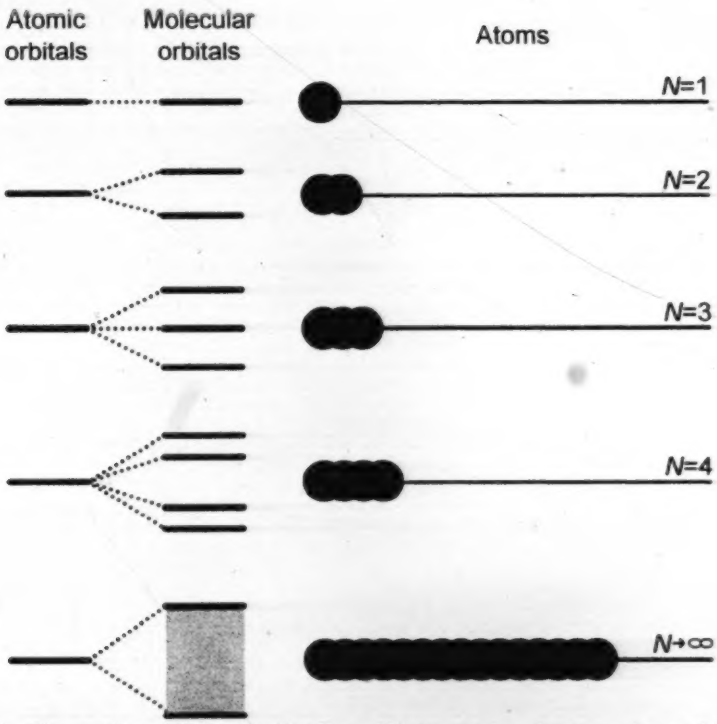

Figure 1 Formation of bands from multiple atoms that are brought into the bonding assembly. As the number (N) of atoms bonded together becomes large, a pseudo-continuous band consisting of N different molecular orbitals of similar energy are formed. (Adapted from reference 2.)

1.1.2.2. Band Structure of Semiconductors

Similar to the analogy used to understand the theory behind bonding and antibonding molecular orbitals (described in MO theory), the orbitals on a semiconductor and an insulator can be separated into two different bands based on the energy level. The low energy orbitals, including the highest occupied molecular orbital (HOMO), are commonly referred to as the *valence band* (VB). The high energy orbitals, including the lowest unoccupied molecular orbital (LUMO), are termed the *conduction band* (CB). The energy difference between the VB and CB is commonly referred to as the band gap (E_g). The Fermi level in a semiconductor is located in the middle of the bandgap between

the top of the VB and the bottom of the CB at $T = 0$ K.[2,3] A simplified pictorial representation of VB and CB is shown in Figure 2.

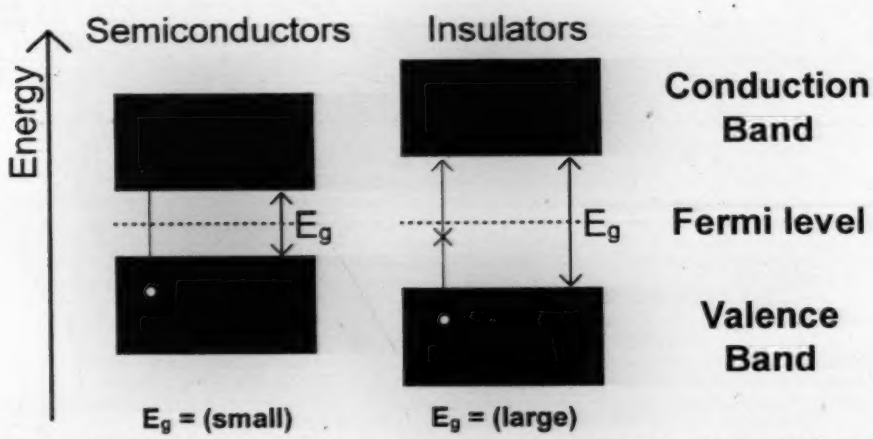

Figure 2 Band structure of a semiconductor and an insulator. (Adapted from reference 2.)

1.1.2.3. Occupation of Orbitals and Electrical Conductivity

The electrical conductivity of a material is commonly classified based on the extent of charge carrier[i] movement within that material (*i.e.*, the conductivity is dependent on how the valence electrons of an atom are able to move throughout the material).[4] The valence electrons in metals are loosely bonded to the atom, allowing them to move freely within the material; in contrast, the valence electrons in insulators are more tightly bonded to the atom, leading to a greater resistance in electron flow.

The conductivity of semiconductors can be determined by the number of electrons promoted across the band gap (E_g).[1,2] Each atom bonded to the bonding assembly (see Section 1.1.2.1) contributes two electrons to the orbitals that formed the CB and VB.[2] When the temperature is above absolute zero, the population distribution of electrons at

[i] Charge carriers are free particles that carry an electrical charge. In a semiconductor, empty electron vacancies (holes) and electrons are treated as charge carriers.

different energy levels can be estimated by the Fermi-Dirac distribution.[ii] At $T = 0$ K, the VB is filled with electrons and is effectively separated from the empty orbitals of the CB. As the temperature is increased ($T > 0$ K), electrons are thermally excited and can begin to populate the empty orbitals at the lower edge of the CB, leaving empty orbitals in the VB. As a consequence, electrons are free to move in the CB, and the electron vacancies, or holes (h^+), may move freely in the VB whenever bias is applied. As temperature increases, more electrons are promoted to the CB, and a semiconductor becomes more conductive.

Semiconductors have photoconductive properties which are controlled by absorption of electromagnetic radiation, such as visible light, x-rays, or UV light. Radiation that can provide sufficient energy to excite electrons from the VB across the band gap into the CB will promote electron movement across the two bands. As is observed with thermal excitation, when more electrons are promoted, the number of free charge carriers increases, and the material becomes more conductive. When the radiation source is removed, electrons do not have sufficient energy to remain promoted across the band gap to the CB, recombination occurs and conductivity decreases.

This carrier movement is illustrated in Figure 3.

[ii] The Fermi-Dirac distribution[1-3] is an estimate of the probability of occupancy of a specific energy state by an electron at any given temperature.

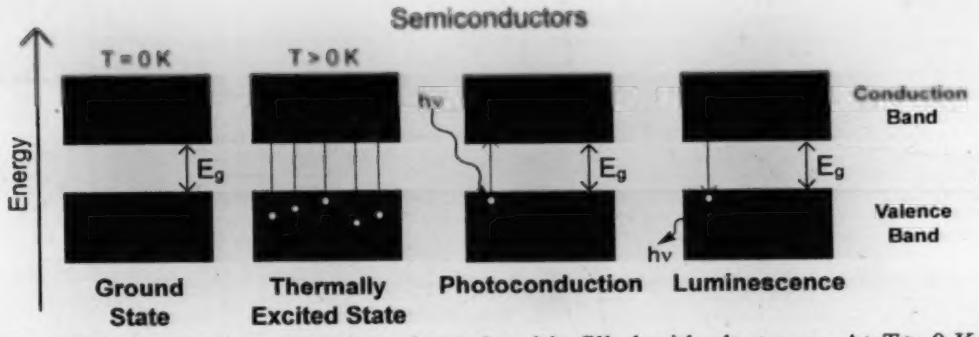

Figure 3 At $T = 0$ K, only the valence band is filled with electrons. At $T > 0$ K, conduction occurs when electrons excited by thermal or photon energy are raised across the energy gap (E_g) forming charge carriers. The positive carrier is the electron hole in the valence band; the negative carrier is the electron in the conduction band. Luminescence occurs when an energized electron in the conduction band returns to the hole in the valence band. A photon of light may be released when the electron drops across the energy gap.

1.1.3. Classification of Semiconductors

Semiconductors can be classified based on their composition and band structure. These two properties can significantly influence reactivity and optical response.

1.1.3.1. Compound vs. Elemental

Compound semiconductors are generally group II-IV or group III-VI (from the periodic table), including GaAs, InSb, and CdSe. Their applications range from solar cells[5] to quantum dot labelling[6] to radiation detectors[7] such as lead sulfide infrared detectors.[8] Elemental semiconductors include germanium and silicon: germanium is used to manufacture transistors and nuclear radiation detectors; silicon is readily used to manufacture computer chips and solar cells.[9]

1.1.3.2.Indirect vs. Direct Band Gap

Semiconductors are also commonly classified on the basis of their band structure and band gap energy because these two characteristics strongly influence semiconductor optical properties. When a semiconductor absorbs energy (*e.g.*, electromagnetic radiation in the form of visible light), an electron is promoted from the VB to the CB (see Section 1.1.2.3). When the excited state "relaxes," it must release energy in the form of heat or light (See luminescence illustrated in Figure 3). For an optical transition (that is, the emission of light) to occur, specific selection rules[iii] must be obeyed.

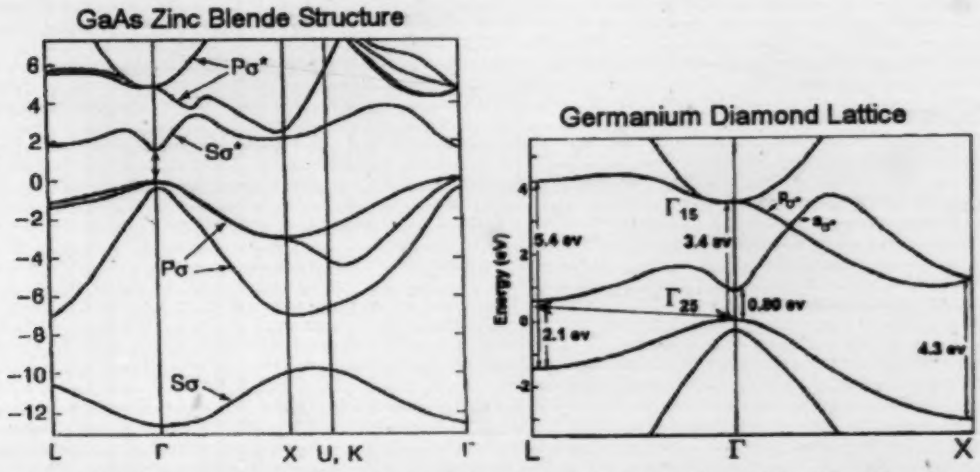

Figure 4 Arrows show examples of direct band gap (left) and indirect band gap (right) energy transitions. Left: Band diagram of a direct gap semiconductor: gallium arsenide. The direct band gap ($\Gamma \rightarrow \Gamma$) absorption is present in the Γ orientation of the crystal lattice. (This article was published in Semiconductors and Semimetals, Volume 49, Brus, L., Silicon Polymers and Nanocrystals, 303 – 328, Copyright Academic Press, 1998.)[10] Right: Band diagram of an indirect band gap semiconductor: bulk germanium. The indirect band gap ($\Gamma \rightarrow$ L) absorption is present. (Reprinted with permission from Wilcoxon, J. P.; Provencio, P. P.; Samara, G. A.; *Physical Review B*, 64, 035417. Copyright 2001, by the American Physical Society.)[11]

[iii] Selection rules identify which energy transitions are allowed because the transitions conserve angular momentum upon an emission or absorption of a photon.[2]

For an *indirect bandgap* semiconductor, the lowest energy point in the conduction band does not occur at the same momentum space coordinate as the highest energy point in the valence band. As a result, the vertical band gap optical transition violates the selection rule requiring conservation of momentum. For this transition to occur in an indirect band gap semiconductor, the emission of a photon must be accompanied by a lattice vibration (phonon).[10] In this way, the selection rule is satisfied. A physical manifestation of this is that bulk crystals of indirect band gap semiconductors, such as Si and Ge, do not photoluminesce at room temperature and are characterized by slow carrier dynamics.[12]

In contrast, the excited state of a *direct bandgap* semiconductor may emit electromagnetic radiation in the form of visible light upon returning to the ground state electronic configuration. This process satisfies the selection rules because the highest point in the valence band and the lowest point in the conduction band occur at the same wave vector in reciprocal space.

1.2. From Atoms to Structures

The discussion above showed that band structure is built by bringing atoms and orbitals together. Quantum confinement in semiconductors is the reverse of this process.

1.2.1. Quantum Confinement

When atoms are removed from bulk material, changes in the electronic structure are insignificant because of the vast number of atoms and orbitals present; however, when particles are smaller, the loss of orbitals is significant and will change the optical

and chemical properties of the particle.[4] The pseudo-continuous bands of large (ca. 1 micron) particles with discrete energy levels will become discontinuous energy bands with unoccupied energy states. This process is illustrated schematically in Figure 5 and is the reverse of the process shown in Figure 1.

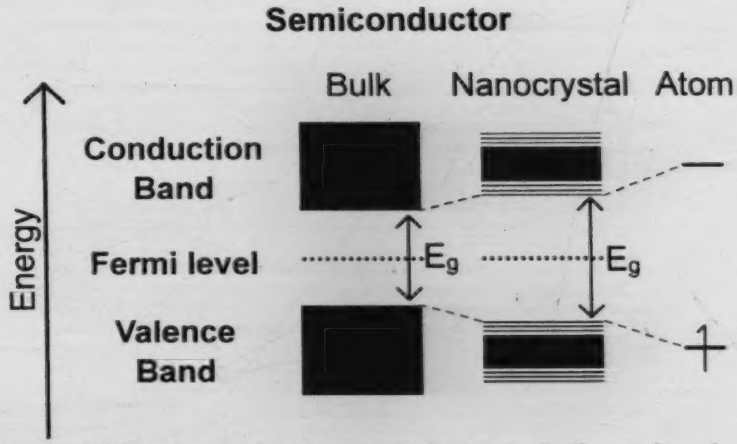

Figure 5 Difference in band patterns between bulk semiconductors, nanocrystal semiconductors, and atoms. (Adapted from reference 13.)

One physical manifestation of this change in electronic structure can be seen in the optical band gap transition of semiconductors. As particle size decreases, an increase in band gap energy results from the removal of atoms. This change in band gap energy results in size-dependent emission properties (see Figure 6).[14-16] The band gap can be correlated with the diameter of the semiconductor and nanoparticle exciton radius in the bulk material. Furthermore, it has been suggested that the selected sizes of nanoparticles can exhibit emissions that cover the range of the visible spectrum,[17] and the wide size distribution of nanoparticles can exhibit excitation wavelength-dependent photoluminescence.[18-21] This behaviour is also observed in Si and Ge.[22,23] Incidentally, because of the large surface area to volume ratio, any changes made to the surface

chemistry of the nanoparticle can change the energy level of the HUMO and LUMO gap.[19]

Figure 6 demonstrates the size-dependent emission properties of CdSe/ZnS nanoparticles. As the diameter of the nanoparticle increases, the band gap decreases, causing the emission to shift to a lower energy; hence, a red shift in the photoluminescence is observed. As the diameter of the nanoparticle decreases, quantum confinement effects dominate, and the band gap increases, causing the emission to shift to a higher energy; hence, a blue shift is observed.

Figure 6 Size-dependent emission of (HDA)-TOPO-TOP (hexadecylamine-trioctylphosphine oxide-trioctylphosphosine) capped CdSe/ZnS nanoparticles.[14] Depending on their size, nanoparticles can emit in the whole visible spectra region with a quantum efficiency of 40 to 70%. (Reproduced with permission from Rogach, A. L.; Talapin, D. V.; Shevchenko, E. V.; Kornowski, A.; Haase, M.; *Adv. Funct. Mater.*, **2002**, 12(10), 653-664. Copyright 2002, Wiley InterScience.)

1.2.2. 0-D, 1-D, 2-D Semiconductor Structures

Nanostructures are often classified in terms of zero dimensions, one dimension, and two dimensions. A dimension is defined as a direction of bulk size (> 1 micron).[4]

- If the size of the bulk material is reduced in one direction only, leaving the exciton[iv] to move freely in two dimensions, the confined structure is called a thin film or a quantum well (QW).
- If two of the three directions of the bulk material are reduced, leaving the exciton to move freely in one direction only, the confined structure is called a quantum wire (QWR).
- If the size of the material is reduced in all directions, and the exciton cannot move freely in any direction, the confined structure is called a quantum dot (QD).

A pictorial representation of these structures is presented in Figure 7.[4]

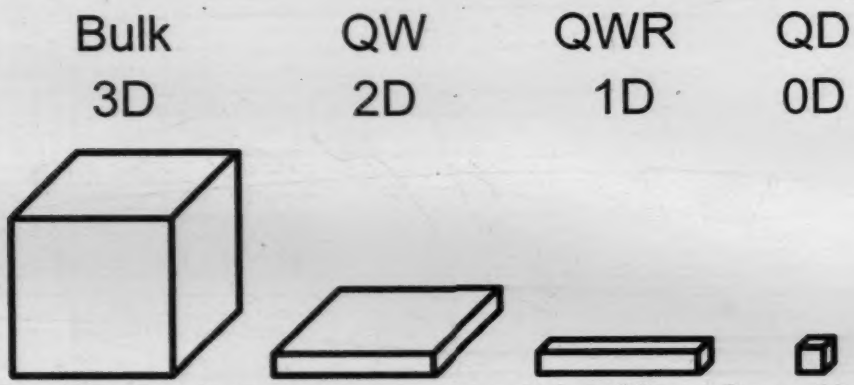

Figure 7 Semiconductor quantum structures. (Adapted from reference 4.)

1.3. Current Semiconductor Nanocrystal Research

1.3.1. CdS and CdSe Nanoparticles

CdS and CdSe nanoparticles have been researched extensively because of their ease of synthesis and unique properties.[14-16, 24-26] These materials serve as model compounds for preparing functional nanomaterials. Current areas of research for these

[iv] An exciton is composed of an electron (e^-) and hole (h^+) pair. The hole is an empty orbital where the excited electron is at its ground state.

materials cover size-dependent emission,[14-16] tailoring shape,[24-26] surface chemistry,[27] and core-shell nanoparticles.[24] CdSe nanoparticles can be synthesized following Scheme 1.[15]

$$Me_2Cd + TOPSe \xrightarrow{TOPO\text{-}TOP} CdSe\text{-}NP + C_2H_6$$

Scheme 1 Method to synthesize CdSe nanoparticles employed by Murray *et al.*[15] TOP/TOPO-capped CdSe can be synthesized by the decomposition of dimethylcadmium (Me_2Cd) and trioctylphosphine selenide (TOPSe) in the presence of a coordinating solvent trioctylphosphine (TOP) and trioctylphosphine oxide (TOPO) and heated to ~ 300°C under 1 atm of argon.

1.3.1.1. Size-Dependent Properties

It is well established that CdSe nanoparticles exhibit size-dependent emission properties.[14] Surface passivation and tailoring the experimental conditions are two methods used to narrow size distribution. It has been reported that near monodisperse (<5% root mean squared in diameter) CdSe nanoparticles can be synthesized with a size range of approximately 1.2 to 11.5 nm; the monodispersity of CdSe can be further improved by passivation of the surface with ZnS forming a composite quantum dot.[15] Narrower size distributions are important for nanoparticle luminescence that requires pure emission in color.[28] Figure 6 is a pictorial representation of size-dependent emission properties of CdSe nanoparticles. Figure 8 contains a collection of the optical absorption spectra of CdSe nanoparticles with sizes ranging from 1.2 to 11.5 nm. A red shift of the emission of the nanoparticle occurs as the size of the CdSe nanoparticle increases.

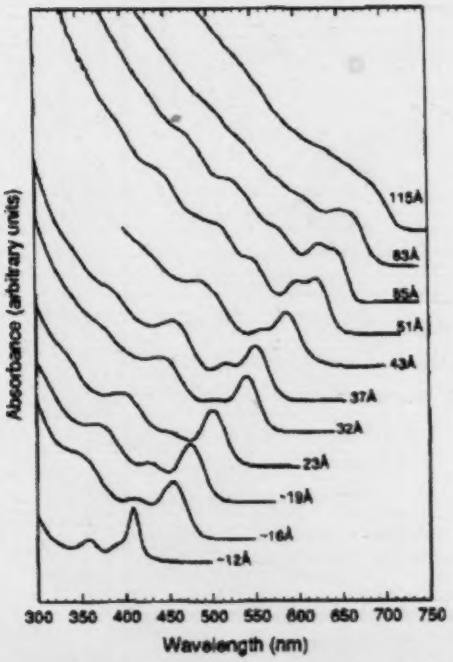

Figure 8 Optical absorption spectra of CdSe nanoparticles in many different sizes. The nanoparticles were dispersed in hexane, and the collection of data was done at room temperature. (Reproduced with permission from Murray, C.B.; Norris, D. J.; Bawendi, M. G.; *J. Am Chem. Soc.*, 115, 8706-8715. Copyright 1993, American Chemical Society.)[15]

1.3.1.2. Possible Shapes of CdSe Nanoparticles

CdSe nanoparticles can also be prepared in different shapes, such as pseudo-spherical nanocrystals, nanorods (See Figure 9), arrows, and tetrapods (see Figures 10, and 11).[24-26, 28] Rods can be grown using simple bench-top techniques as outlined in Scheme 2.[25] The synthesized CdSe nanorods or quantum rods have lengths varying from 7.5 to 40.0 nm and diameters ranging from 3.0 to 6.4 nm.[24] The preparation and characterization of CdS/ZnS core/shell nanorods were studied to determine how size and shape can have an influence on structural strains of the nanorod.[25] It was also

demonstrated that CdSe can be ordered into 3D nanostructures by self-assembly (see Figure 12).[28]

$$Se_{(s)} + Cd(CH_3)_2 + TBP \xrightarrow[TOPO]{HPA,\ TDPA} \underset{(rods)}{CdSe\text{-}NP} + C_2H_6$$

Scheme 2 Method to synthesize CdSe nanoparticles employed by Manna *et al.*[22] The selenium powder and dimethylcadium precursors were dissolved in tri-*n*-butylphosphine (TBP) and injected into a mixture of hexylphosphonic acid (HPA), tetradecylphosphonic acid (TDPA), and trioctylphosphine oxide (TOPO). The mixture was heated to 360°C, and a mixture of dimethylcadmium dissolved in TBP was added.[25]

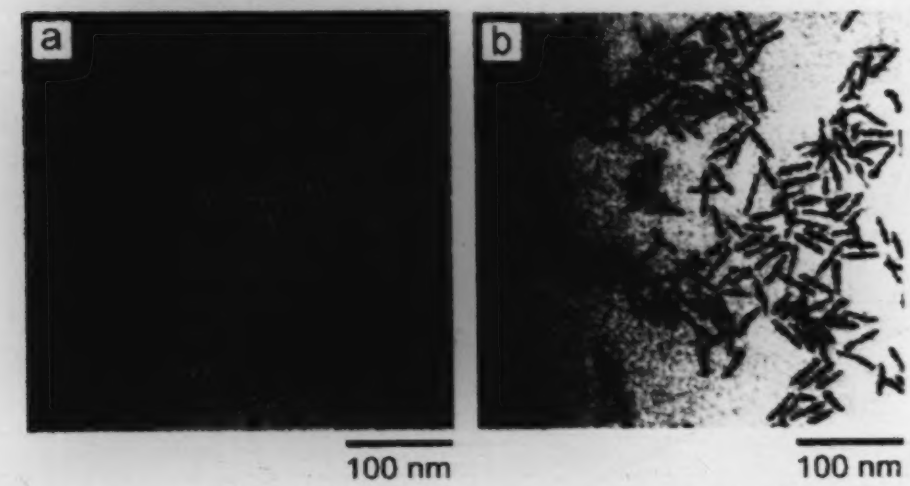

Figure 9 Transmission electron micrographs of CdSe nanorods in (a) short (5.0 × 18.0 nm) and (b) long (4.5 × 36.0 nm) sizes. (Reproduced with permission from Manna, L.; Scher, E. C.; Li, L. S.; Alivisatos, A. P.; *J. Am. Chem. Soc.*, 124, 7136–7145. Copyright 2002, American Chemical Society.)[25]

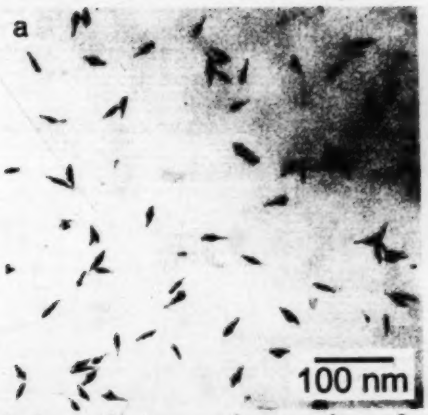

Figure 10 Transmission electron micrographs of CdSe teardrop-shaped nanoparticles. (Reproduced with permission from Manna, L.; Scher, E. C.; Li, L. S.; Alivisatos, A. P.; *J. Am. Chem. Soc.*, 124, 7136–7145. Copyright 2002, American Chemical Society.)[26]

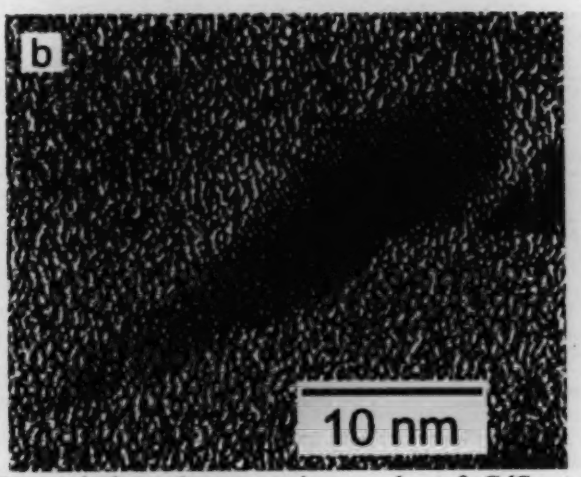

Figure 11 Transmission electron micrographs of CdSe teardrop-shaped nanoparticles. (Reproduced with permission from Manna, L.; Scher, E. C.; Li, L. S.; Alivisatos, A. P.; *J. Am. Chem. Soc.*, 124, 7136–7145. Copyright 2002, American Chemical Society.)[26]

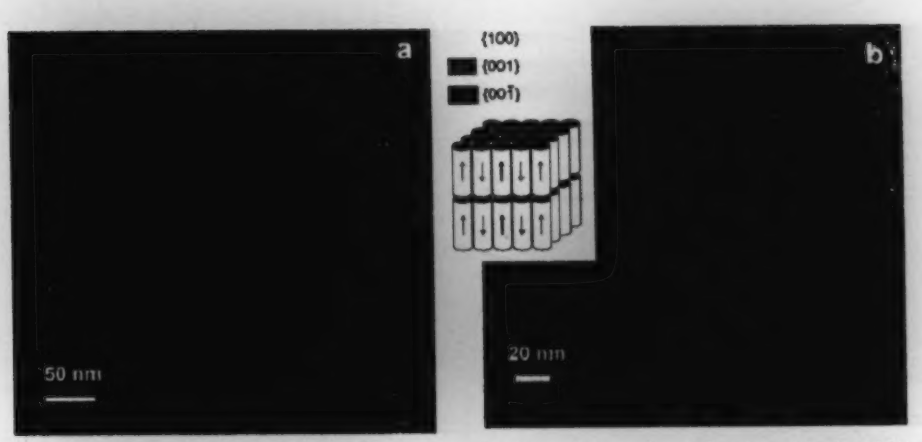

Figure 12 Transmission electron micrographs of self-assembled CdSe nanorods in (a) tracks and (b) superstructures. The insert in (b) shows the antiparallel dipole pairing of the CdSe nanorods, which is the preferred orientation. (Reproduced with permission from Talapin, D. V.; Shevchenko, E. V.; Murray, C. B.; Kornowski, A.; Förster, S.; Weller, H. J.; *Am. Chem. Soc.*, 126, 12984–12988. Copyright 2004, American Chemical Society.)[28]

1.3.1.3. Surface Chemistry

It is necessary to "cap" semiconductor particles if particle aggregation is to be minimized. By capping the vacant bonding sites on the surface of the nanoparticle with stabilizing agents or surfactants, the size of the nanoparticle can be controlled because particle agglomeration cannot take place.[27] The surface of the nanoparticle is also protected from oxidation because the nanoparticle is not exposed to harsh environments that could cause it to decompose.[29] The ability to tailor the surface chemistry of the nanoparticle also allows for the fine tuning of emission properties. This is done by electronically trapping electrons within surface-functionalized nanoparticles.[14-16] Common stabilizing agents used to cap CdSe nanoparticles include tri-*n*-octylphosphine oxide-tri-*n*-octylphosphine TOPO-TOP (see Scheme 1), hexadecylamide (HDA)-TOPO-TOP mixture (see Scheme 3), thiolalcohol, and thioacid-stabilized and -capped CdSe.[27,29]

$$Me_2Cd + TOPSe \xrightarrow[HDA]{TOPO\text{-}TOP} CdSe\text{-}NP + C_2H_6$$

Scheme 3 A method of preparing (HDA)-TOPO-TOP-capped CdSe nanoparticles employed by Rogach *et al.*[14] The hexadecylamide tri-*n*-octylphosphine oxide-tri-*n*-octylphosphine (HDA-TOPO-TOP) capped CdSe nanoparticle is synthesized by dissolving TOPSe and Me_2Cd into TOP, then adding TOPO and HDA. The mixture is then heated to 300°C to promote crystal growth. The addition of an acidic component, *n*-tetradecyl phosphonic acid (TDPA), can further minimize the size distribution.

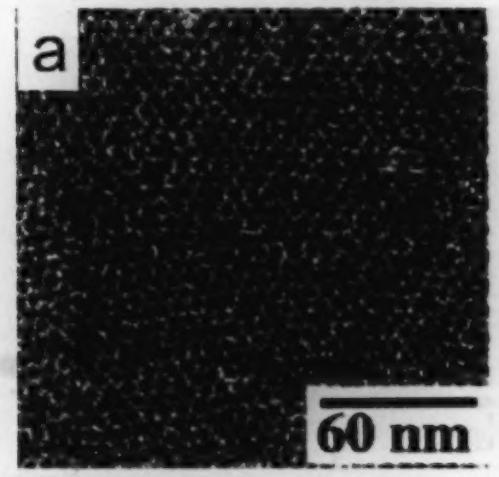

Figure 13 Transmission electron micrographs of TDPA-HDA-TOPO-TOP-capped CdSe nanoparticles synthesized following Scheme 3. (Adapted from reference 14 [used with permission].)

An alternative method to cap CdSe nanoparticles is discussed in the following section.

1.3.1.4. Multiple Core/Shell Nanoparticles

Attempts have been made to improve the stability of the nanoparticles and enhance their photoluminescence (PL) by growing a thin shell of a semiconductor on the outer surface of an emitting nanoparticle.[24] It is known that a ZnS-coated CdSe nanoparticle can be made following the reaction in Scheme 4. The (CdSe)ZnS

nanoparticles synthesized following the method outlined in Scheme 4 are near monodisperse with sizes ranging from 2.3 to 5.5 nm. The ZnS monolayer measures 0.31 nm. The photoluminescence spectra of a CdSe(ZnS) nanoparticle exhibits a red shift in the absorption spectra.[16] The red shift is more obvious when the size of the CdSe nanoparticles is larger because of partial leakage of the CdSe exciton into the ZnS shell caused by quantum confinement; hence, a more dynamic effect is observed (see Figure 14).

$$CdSe \xrightarrow[(TMS)_2S]{ZnEt_2} (CdSe)ZnS + (TMS)_2Et_2$$

Scheme 4 Synthesis of (CdSe)ZnS nanoparticles employed by Dabbousi *et al.*[16] The CdSe nanoparticles passivated with TOPO are mixed with diethylzinc ($ZnEt_2$) and hexamethyldisilathiane $(TMS)_2S$ at the desired temperature to form a ZnS-overcoated CdSe quantum dot.

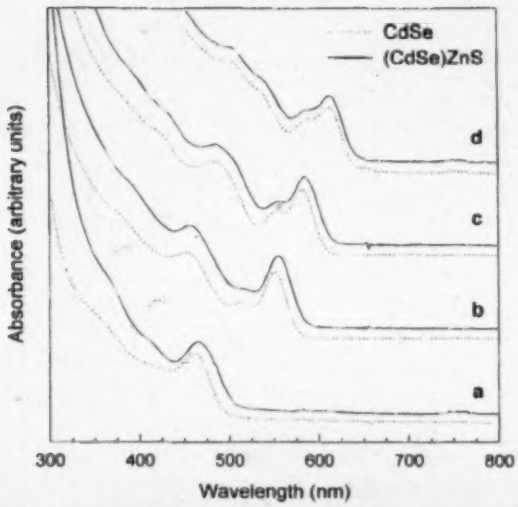

Figure 14 Absorption spectra for one- or two-monolayer ZnS-coated CdSe nanoparticles (solid lines) and bare CdSe nanoparticles (dashed lines). CdSe nanoparticles have diameters measuring (a) 2.3 nm, (b) 4.2 nm, (c) 4.8 nm, and (d) 5.5 nm. (Reproduced with permission from Dabbousi, B. O.; Rodriguez-Viejo, J.; Mikulec, F. V.; Heine, J. R.; Mattoussi, H.; Ober, R.; Jensen, K. F.; Bawendi, M. G.; *J. Phys. Chem. B*, 101, 9463–9475. Copyright 1997, American Chemical Society.)[16]

Multishell CdSe/CdS/ZnS and CdSe/ZnSe/ZnS core/shell/shell nanoparticles are also well known.[30] It is believed that the outer shell provides photochemical stability, and the middle shell reduces strain within the nanocrystal because the lattice structure of the middle shell acts as a bridging lattice between the core and outer shell of the nanoparticle.[24] For this example, CdSe/ZnSe and CdSe/ZnSe/ZnS are synthesized using the same CdSe core described in Scheme 5. Characterization of the multishell nanoparticle indicates that by growing a ZnS shell around a CdSe/ZnSe nanoparticle (see Figure 15), a small red shift in absorption will result (see Figure 16). Furthermore, increasing the thickness of the outer ZnS shell of a CdSe/ZnS nanoparticle from two to four monolayers leads to a decrease in photoluminescence of the resulting nanoparticle

(see Figure 17). This is in contrast to a CdSe/ZnSe/ZnS nanoparticle; in this case, a decrease in PL is less obvious when there is a change in the thickness of the ZnS shell. CdSe/ZnSe/ZnS nanoparticles are also believed to exhibit higher PL (5 to 10%) compared with CdSe/CdS/ZnS nanoparticles.

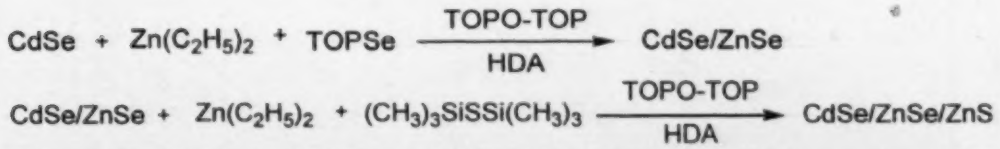

Scheme 5 Synthetic pathways of CdSe/ZnSe/ZnS nanoparticles employed by Talapin *et al.*[30] CdSe/ZnSe nanoparticles are prepared by adding HDA-TOPO-TOP-capped CdSe to a ZnSe solution made using $Zn(C_2H_5)_2$ and TOPSe. The stock solution of ZnS is prepared by mixing $Zn(C_2H_5)_2$ with $(CH_3)_3SiSSi(CH_3)_3$ (bis[trimethylsilyl]sulphide) and adding this mixture to a solution of CdSe/ZnSe at 200 to 220°C.[30]

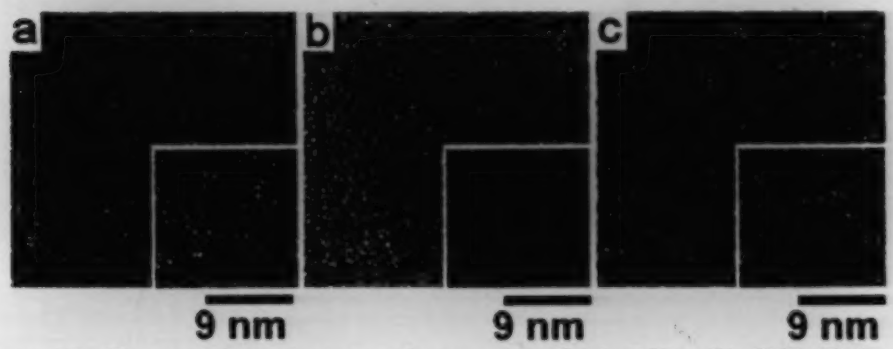

Figure 15 Transmission electron micrographs of (a) CdSe, (b) CdSe/ZnSe, (c) CdSe/ZnSe/ZnS nanoparticles grown following Scheme 5. (Reproduced with permission from Talapin, D. V.; Mekis, I.; Götzinger, S.; Kornowski, A.; Benson, O.; Weller, H.; *J. Am. Chem. Soc.*, 26, 18826-18831. Copyright 2004, American Chemical Society.)[30]

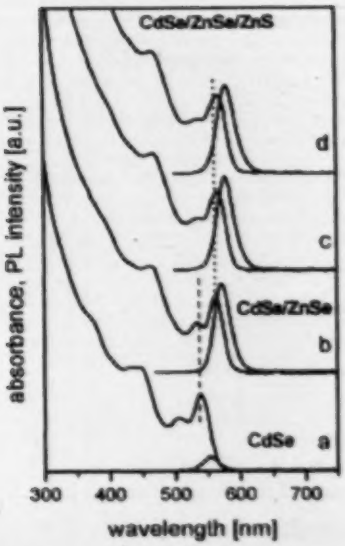

Figure 16 Absorption spectra for (a) CdSe nanoparticles, (b) CdSe/ZnSe (core/shell) nanoparticles (ZnSe ~ 2 monolayers of thickness), (c) CdSe/ZnSe/ZnS (core/shell/shell) nanoparticles (ZnS ~ 2 monolayers of thickness), and (d) CdSe/ZnSe/ZnS (core/shell/shell) nanoparticles (ZnS ~ 4 monolayers of thickness). (Reproduced with permission from Talapin, D. V.; Mekis, I.; Götzinger, S.; Kornowski, A.; Benson, O.; Weller, H.; *J. Am. Chem. Soc.*, 126, 18826-18831. Copyright 2004, American Chemical Society.)[30]

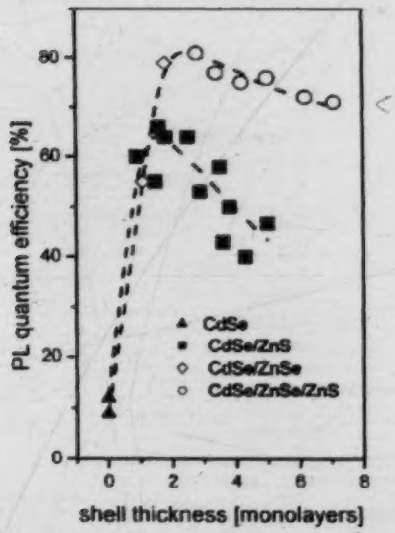

Figure 17 Effect that shell thickness has on PL quantum efficiency on various monolayers of multiple-shell CdSe nanoparticles. (Reproduced with permission from Talapin, D. V.; Mekis, I.; Götzinger, S.; Kornowski, A.; Benson, O.; Weller, H.; *J. Am. Chem. Soc.*, 126, 18826-18831. Copyright 2004, American Chemical Society.)[30]

1.4. Synthesis of Surface-Functionalized Group IV Semiconductor Nanoparticles

Despite all the advances in semiconductor nanoparticle synthesis mentioned previously, studies of silicon and germanium quantum dots remain in their infancy. Although germanium and silicon are in the same periodic group, their chemistry and reactivity differ, and techniques that have been developed may not be interchangeable. To date, few of the examples noted above for Si surface reactivity have been applied to Ge or Ge nanoparticles, or vice versa. Efficient methods for preparing these materials are still being developed and size-dependent properties still challenge modern theories.

1.4.1. Particle Synthesis

There are many different techniques for preparing Group IV semiconductor nanoparticles.[31-50] One major challenge in preparing group IV nanoparticles is their inherent instability in atmospheric conditions. When particles are exposed to atmospheric conditions, they are susceptible to surface oxidation.[11] Conceivably, tailoring surface chemistry can protect the nanoparticles from surface oxidation. A favourable method for tailoring the surface chemistry of Group IV semiconductor nanoparticles bearing hydride surface termination is to exploit known hydrometallation procedures.[31] Another attractive approach reported in the literature involves the use of organic capping agents, such as Grignard reagents, alkyl lithium, and other terminal groups, to tailor the surface of the nanoparticles.[32-34] With the introduction of ambient stability resulting from surface functionalization, other important variables, such as size and shape, can be addressed effectively. While there is much research into Si nanoparticle synthesis and modification, Ge nanoparticle chemistry is much less developed.[6]

1.4.2. Surface Functionalization

Because nanoparticles are unstable compared to their bulk counterparts, it is important to develop methods to stabilize their surface.[34] A monolayer of organic material at the nanoparticle surface can provide protection from exposure to degrading conditions, including oxidation.[35] Quenching light emission from porous silicon can be achieved through the introduction of groups such as phenethynyl, styrenyl, and

halogens.[31] Furthermore, because silicon and germanium are very sensitive to oxidation, it is necessary to protect the surface as soon as the nanoparticles are synthesized.[35]

1.4.3. Synthesis of Germanium Nanoparticles.

Solution-based approaches for germanium nanoparticle synthesis include reduction of GeX_4 using reducing agents such as lithium naphthalide (X = Cl),[32] NaK (X = Cl),[33] Mg_2Ge (X = Cl),[34] and $LiAlH_4$ (X = Cl, Br, and I),[11] as well as thermolysis reactions (reduction of GeI_2).[35] One method of tailoring the surface chemistry of germanium is known as hydrogermylation. Hydrogermylation is the process of inserting a C=C bond into a surface-bonded Ge-H bond which results in the formation of a Ge-C bond.[31]

Germanium nanoparticles have been synthesized using germanium tetrachloride and lithium naphthalide (see Scheme 6).[32] It was suggested that particle stability and limited particle size were controlled by capping the dangling bonds at the surface of the germanium nanoparticle with $(CH)_3Si$. TEM analyses showed that the resulting nanoparticles were amorphous and have a broad size distribution with an average diameter of 2.0 nm. It was concluded that the germanium nanoparticles are terminated with R_3Si groups based solely on support from the energy-dispersive x-ray spectrum (EDX) that indicates the presence of germanium and silicon. It was discovered that, upon exposure of the redissolved amorphous particles to a ruby laser, the size of the particles increased and the particles became more crystalline.

$$n\,GeCl_4 + 4n\,Li[C_{10}H_8] \longrightarrow Ge_n + 4n\,C_{10}H_8 + 4n\,LiCl$$

Scheme 6 Germanium tetrachloride reduced in solution with lithium naphthalene, yielding germanium nanoparticles.[32] An organic methyl group (Me_3SiCl) is used to terminate dangling bonds on the surface of the germanium nanoparticle.

Yet another reductive approach to making germanium nanoparticles is shown in Scheme 7.[33] The mechanism for this reaction consists of three standard separate steps:

1. Reduction: NaK alloy was used to reduce $GeCl_4$ to yield elemental germanium, sodium chloride, and potassium chloride.
2. Nucleation: Upon reduction, Ge clusters nucleated and crystallized when the reaction mixture was heated until it reached 270°C, which took 24 to 48 hours. The excess reagents present in the reaction were believed to be needed to promote epitaxial[v] growth onto the nanoparticles, thereby increasing particle size.
3. Crystallization of Ge clusters: This synthetic method provides crystalline germanium nanoparticles with a broad diameter distribution ranging from 5.5 to 8.0 nm. X-ray powder diffraction (XRD) data confirm a diamond lattice crystal structure and the presence of GeO_2.

IR analysis of the germanium nanoparticles supports an oxide (GeO_2) surface with some Ge-Cl termination. TEM electron energy loss spectroscopy (EELS) studies confirmed that the surface of the nanoparticle is passivated with GeO_2 as indicated by surface plasmon energy of ~ 7.1 eV, which suggests a transition of GeO_2 from a localized Ge-O antibonding state to a conduction band energy state where electrons are delocalized and Ge-Ge interactions are present.

---

[v] Epitaxial growth describes the growth of atom-sized layers onto the surface of a substrate. The substrate can be in the form of a crystal or on the surface as a thin film.

While this approach is promising, the need for highly reactive NaK and reduction under a high temperature at 270°C for 24 to 48 hours makes this method impractical and dangerous. In addition, the broad size distribution provided by this method presents challenges in the characterization and eventual understanding of particle electronic structures given the strong disbursement of quantum dot on size, electronic, and optical properties.

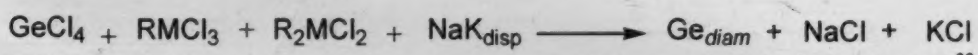

Scheme 7 Method to synthesize germanium particles employed by Heath *et al.*[33] In this reaction, M represents either Ge or Si; R represents any organic functional group. The R group acts as a capping agent to limit the size of the nanoparticles synthesized and to keep the nanoparticles separated. NaK alloy dispersion (in heptane) is used as the reduction agent. Ge_{diam} represents the diameter of Ge.

A single-step reduction method reported by Tanke *et al.* is unique because the reductant serves as a Ge source and a reducing agent. $GeCl_4$ is reduced by magnesium germanide to yield Ge nanoparticles (see Scheme 8).[34] The chloride surface-terminated crystalline germanium nanoparticles produced by this approach have diameters of 4 ± 2 nm and can be further modified with alcohols, acetals, polymer chains, and esters using a variety of methods. While this synthetic methodology affords narrower size distributions than those outlined previously, a full understanding of the photoluminescence (PL) spectroscopy is still difficult to attain because the size distribution of nanoparticles results in broad excitation wavelength-dependent PL spectra.

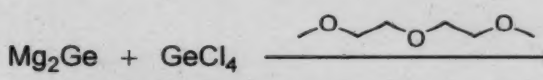

Scheme 8 Germanium nanoparticle synthesis from the reaction of Zintl salt and Mg_2Ge with $GeCl_4$ in the presence of 2-methoxy ethyl ether.[34] The product, Q-Ge-Cl, is Cl-terminated Ge nanoclusters.

Scheme 9 outlines the reduction of germanium tetrahalide (GeX_4, where X = chloride, bromide, and iodide) as the starting precursor.[11] The authors claim that when $LiAlH_4$ is added, Ge(IV) is reduced to Ge(0). They suggested that by varying the concentration of surfactant, the size of the micelles will change; as well, they hypothesized that nucleation and growth of the nanoparticles took place in the hydrophilic interior of micelles formed by surfactants in the reaction. By changing the size of the micelle, the growth of the Ge nanoparticle can be controlled since particle growth is limited to the interior of the micelle. The germanium nanoparticles, with diameters ranging from 2 to 10 nm, were produced and purified by size-exclusion chromatography (SEC). This method might be one of the best for separating nanoparticles into different sizes. Although this method seems very promising, the authors provide no conclusive data regarding tailoring particle size or surface chemistry. Furthermore, they incorrectly identified that the vigorous bubbling that occurred when $LiAlH_4$ was added was due to the rapid release of H_2. A similar reaction, the reduction of $SiCl_4$ by $LiAlH_4$, has been known for some time, and the products were SiH_4, LiX, and AlX_3.[37] Still, this method holds promise if the reaction conditions could be optimized to afford narrower size distribution and the surface chemistry could be controlled.

$$GeX_4 + LiAlH_{4\,(s)} \xrightarrow[\text{solvent}]{\text{surfactant}} \text{Q-Ge} + \text{salts} + H_2$$

Scheme 9 Method of germanium nanoparticle (Q-Ge) synthesis described by Wilcoxon *et al.*[11] The X in the reaction represents halogens, including chloride, bromide, and iodide.

An alternative approach in Ge nanoparticle synthesis using GeI_2 is outlined in Schemes 10 and 11.[35] GeI_2 was used because of its higher solubility in organic solvent when GeI_2 was mixed with alkyl phosphine (R_3P) coordinating solvents such as

trioctylphoshine (TOP) to form TOP·(GeI_2). The TOP also serves as a capping agent for the GeI_2 to minimize particle aggregation; thus, particles synthesized are less polydispersed. Furthermore, GeI_2 disproportionates at ~ 330°C, producing GeI_4 and Ge and eliminating the need for a reducing agent.[35,36] Particles synthesized using this method were analyzed using high-resolution transmission electron microscopy (HRTEM) and XRD. TEM micrographs indicate that size control was achieved by changing the GeI_2 concentration. The size of the nanoparticles increased from 8.1 ± 1.4 nm to 11.6 ± 2.2 nm when the concentration of GeI_2 in TOP was increased from 250 to 520 nM. Similarly, a size decrease to 3.0 ± 0.5 nm was achieved when the concentration of GeI_2 in TOP was decreased to 130 nM. XRD confirms the presence of crystalline Ge nanoparticles with diamond cubic structure. Calculated diameters using the Scherrer equation were consistent with TEM measurements. Surface studies using energy-dispersive x-ray spectroscopy (EDS) indicate the presence of Ge with small traces of oxygen, phosphorus, and iodine. FT-IR studies show the presence of CH_2 and CH_3 groups, indicating that hydrocarbons are present. However, there is no indication that hydrocarbon is attached to the surface of germanium.

$$GeI_2 + LiAlH_{4\,(s)} \xrightarrow[300\ ^\circ C\ /\ 1\ h]{(C_8H_{17})_3P} \text{Ge-NP} + AlI_3 + LiI$$

$$GeI_2 + LiAlH_{4\,(s)} \xrightarrow[240\ ^\circ C\ /\ 1\ h]{(C_4H_9)_3P} \text{Ge-NP} + AlI_3 + LiI$$

Schemes 10 (top) and **11** (bottom): Method in preparing germanium nanoparticles described by Lu *et al.*[35] The size of the nanoparticles can be controlled by the concentration of GeI_2 dissolved in the surfactant tri-*n*-octylphosphine (TOP) and tri-*n*-butylphosphine (TBP).

Gerung *et al.*[36] describes a thermal reduction method to make germanium nanoparticles that involved the dissociation of a germanium precursor by heat to initiate a

reaction (see Scheme 12). The size of the nanoparticles investigated via TEM was 7 ± 4 nm, and of the 119 nanoparticles, 95% were less than 8 nm. XRD and high-resolution TEM data show that the germanium nanoparticles are crystalline with d-spacing that matches bulk germanium cubic lattice structures. FT-IR data indicate that GeO_2 is not present; instead the surface was encapsulated with oleylamine ligands because the N-H wagging mode signals and C-N signals were present. While this reaction holds promise, the broad size distribution and the inability to tailor the surface chemistry limit its utility.

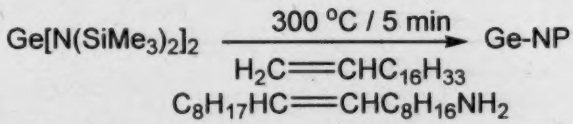

Scheme 12 Thermolysis of Ge precursor, $Ge[N(SiMe_3)_2]_2$, described by Gerung *et al.*[36]

1.4.4. Synthesis of Silicon Nanoparticles

It is known that the surface chemistry of silicon nanoparticles can be tailored to improve nanoparticle stability by providing the ability to control the rate of surface oxidation and the change in solubility characteristics. This then allows for more convenient methods of particle purification.[29] Changes to the surface chemistry of a nanoparticle can have an effect on its electronic structure, specifically the lowest unoccupied molecular orbital (LUMO) energy level. This is because of the high surface area-to-volume ratio. Early synthetic studies on silicon nanoparticles focused on oxide-terminated surfaces[38-39] and made no attempt to tailor the surface chemistry of silicon due to its complexity.[40-41] Subsequent investigation of chemically active surfaces (*e.g.*, Si-Br, Si-H, Si-OH, and Si-Cl), with extensive research in bulk silicon, provides a good foundation for investigation into surface functionalization of silicon nanoparticles.[31]

Tailoring the surface chemistry of silicon nanoparticles was first discovered in the reduction reaction of $SiCl_4$ with potassium silicide (see Scheme 13).[42] Methanol was added to the crude mixture (see Scheme 14) and the silicon products were analyzed. The product of the reduction reaction was originally presumed to be chloride-functionalized silicon nanoparticles; however, it was confirmed from spectroscopy data that the hydrophobic air stable product was terminated by the methoxy group ($-OCH_3$).[42]

$$4n\ KSi + n\ SiCl_4 \xrightarrow{THF} Si\text{-}NP + 4n\ KCl$$

Scheme 13 Solution-based synthesis of silicon nanoparticles described by Bley *et al.*[42] This solution reaction is carried out by refluxing a solution of KSi with excess $SiCl_4$ in the glyme, diglyme, or THF.

$$-SiCl + CH_3OH \longrightarrow -SiOCH_3 + HCl$$

Scheme 14 The surface of the silicon nanoparticle, presumed to be chlorine terminated, was chemically modified by exposure to methanol at room temperature.[42]

The surface chemistry of the Cl-terminated silicon nanoparticles can also be tailored upon exposure to different reagents, such as Grignard and alkyl lithium, or can be reduced by using $LiAlH_4$ with exposure to bromine (see Scheme 15).[43-45]

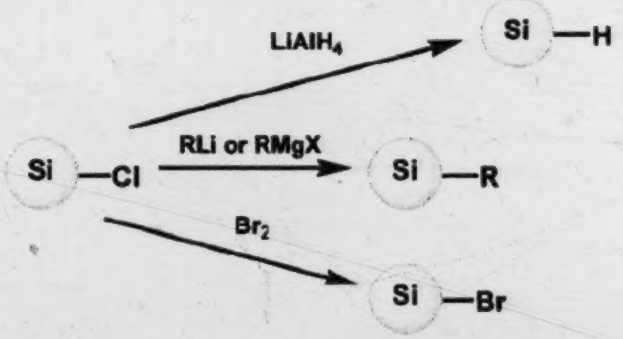

Scheme 15 Solution methods commonly used to tailor the surface of silicon nanoparticles.[43-45] 1. *[Veinot, J. G. C.; Chem. Commun., **2006**, 4160–4168.] – Reproduced by permission of The Royal Society of Chemistry.*

Chloride-terminated silicon nanoparticles have also been prepared by reduction of $SiCl_4$ using sodium naphthalide in the presence of 1,2-dimethoxyethane (glyme).[46-47] The Cl-capped silicon nanoparticles can be further terminated by alkoxy groups (*e.g.*, *n*-octanol) upon exposure to an alcohol (see Scheme 16).

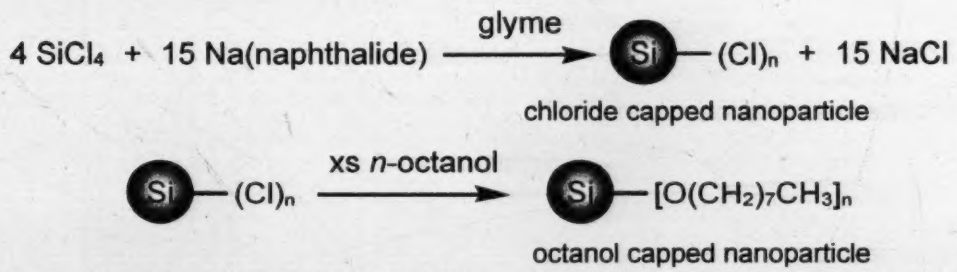

Scheme 16 Reduction of $SiCl_4$ with sodium naphthalide and glyme gives chlorine terminated silicon nanoparticles. Excess n-octanol is added to change the silicon surface termination from Cl to octanol.[46-47]

Hydrofluoric acid can be used to etch away the amorphous layer of silicon oxide encapsulated on the surface of a silicon nanoparticle.[48] By etching away the oxide surface of the nanoparticle using HF and HNO_3 (see Scheme 17), the surface of the silicon nanoparticle will be hydride terminated.[48] Hydrosilylation, a thermo- or photochemically initiated reaction (see Scheme 17) can be used to render the surface of the nanoparticles hydrophobic. As a result, particles become soluble in organic solvents.[49]

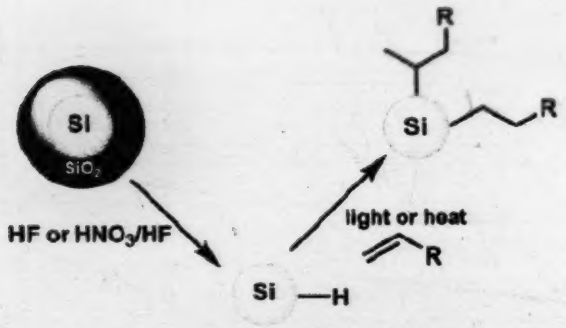

Scheme 17 The oxide layer on an oxide-coated silicon nanoparticle can be removed by etching it away with hydrofluoric acid and nitric acid, thereby forming hydride-terminated silicon nanoparticles.[48] Hydrosilylation can be initiated photochemically in the presence of a terminal alkene.[49-50] *[Veinot, J. G. C.; Chem. Commun., **2006**, 4160–4168.] – Reproduced by permission of The Royal Society of Chemistry.*

A hydride-terminated silicon nanoparticle can also be synthesized by reduction of $SiCl_4$ with $LiAlH_4$, and the surface of the nanoparticle can be stabilized with tetraoctylammonium bromide (TOAB) (see Scheme 18).[48] Instead of hydrosilylation, the surface functionalization is catalyzed by hexachloroplatinic acid (Pt catalyst) in the presence of the terminal alkene (*e.g.*, heptane and allylamine).

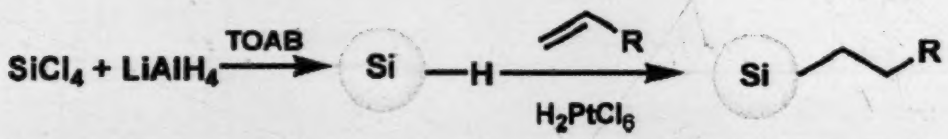

Scheme 18 Reduction of $SiCl_4$ with $LiAlH_4$ which forms a hydrogen-terminated silicon nanoparticle stabilized by tetraoctylammonium bromide (TOAB).[51] Hexachloroplatinic acid (Pt catalyst) and the terminal alkene (*e.g.*, 1-heptene) are added to change the surface of the silicon nanoparticle.[29] *[Veinot, J. G. C.; Chem. Commun., **2006**, 4160–4168.] – Reproduced by permission of The Royal Society of Chemistry.*

1.5. Nanoscience and Nanotechnology

1.5.1. What Is *Nano*?

The word *nano* is derived from the Greek word νάνος meaning "dwarf" or "little old man."[52] It is commonly used to describe a unit of measurement in one billionth (10^{-9}) fractions, with an emphasis on size and length of time, and is usually referred to in physical science-related literature when size is a critical factor.[53]

1.5.2. What Is Nanotechnology?

The basic concept of nanotechnology was proposed by Taniguchi in 1974; Taniguchi defines the accuracy in manufacturing methods and production processes to be in the order of 1 nm.[54] The reason 1 nm was chosen is that the resolution limit in the measurable and confirmable distance between atomic lattices and between atoms is about 0.3 nm.[55] Nanotechnology is sometimes referred to as molecular manufacturing because it involves

- the building or fabrication of electronic circuits and devices in an atomic and molecular scale
- the nano-fabrication of integrated circuits in the nanometric scale, and
- the manipulation and visualization of individual atoms on the surface of a single crystal with precision up to a single atom of an element.[56]

1.5.3. Nano in History

Throughout history many scientists believed that the ability to manipulate anything small was limited by the capabilities of the tools that were available. At the

same time the ability to study particles within a molecular or atomic size regime is limited by the suitability of the instrumentation and techniques. In his famous lecture "There's Plenty of Room at the Bottom" (1959), Prof. Richard P. Feynman predicted that manipulating single atoms and molecules to form ordered, meaningful patterns was achievable.[54] Feynman proposed that it was the lack of appropriate methods, instead of the laws of physics, that limited the possibility of placing single atoms or molecules in the desired locations. Feynman's scientific peers were very familiar with the top-down approaches for making structures using tools that were available. But this approach is limited by the capabilities of the tools employed to make a structure. (For example: When removing material in a similar way to cutting a piece of wood with a chisel, one would use a proper-sized chisel in order to obtain the same precision. As the size of the piece of wood decreases, a smaller chisel is used to carve the wood. But there comes a time when the piece of wood and the chisel become so small that it is impractical to carve a piece of wood to obtain the correct size.) Feynman outlined a bottom-up approach that involves using macro-scale components built from single molecules. This technique can be used to design and build instruments that allow characterization at the atomic level.

Forty-five years after Feynman's famous address, technology was in place to study and manipulate atoms and molecules individually. One of these revolutionary methods is scanning probe microscopy, which allows researchers to position single atoms and/or molecules in their desired place. Another revolutionary method is transmission electron microscopy (TEM), a dimension analysis device that can provide researchers with a visual image of the particle in the nanometre size regime. Feynman's prediction regarding the ability to position and study individual atoms was realized.

1.5.4. Nano in Science

Recent developments of nanotechnology in the modern world involve multiple scientific disciplines, and examples of these developments are listed below. One area of particular interest is optimizing nanoparticle synthesis, which includes understanding their unique properties, control and manipulation, characterization, and applications.

1.5.4.1. Carbon Nanotubes

Carbon nanotubes (CNT) were first discovered by Sumio Iijima in 1991 when he was investigating the synthesis of C_{60} as well as other fullerenes using the arc-discharge evaporation method.[57] The arc-discharge method involves applying a direct current (DC) voltage between two separated graphite rods in an inert gas environment. The CNTs are recovered from a small quantity of the evaporated anode deposited on the cathode end of the two electrodes. Other reported methods for producing CNT include laser ablation and plasma torch.[58] Some of the applications of CNT include electronic devices[59] and chemical sensors.[60]

1.5.4.2. Porous Silicon

Porous silicon (PS) was discovered by Uhlir[61] in 1956, but its optical properties were not reported until 1990 when L. T. Canham investigated the luminescent properties of electrochemically etched porous silicon wafer.[62] As the porosity of the Si wafer increases, the photoluminescence intensifies, and the emission shifts from the near infrared region to the visible region (bright red). Porous silicon can be obtained by

anodization[vi] using HF[63] or stain etching using HF, HNO_3, and water.[64] Porous silicon, prepared in an electrochemical cell by anodization of dissolution of HF, is used as a gas sensor,[65] which allows the detection, in low concentrations, of HCl,[66] NH_3 (500 ppb), CO (< 5 ppm), NO_x (< 1 ppm), and SO_2 (< 1 ppm).[67]

1.5.4.3. Other Elemental Nanoparticles and Their Applications

Currently, scientists have expanded their nanoparticle research to other elements, such as silver. Many processes that can transform elemental silver into particles of micron to sub-micron sizes have been reported. Some reported techniques include ultrasonic spray pyrolysis of aqueous silver nitrate, forming silver nanoparticles larger than 20 nm;[68] and photo reduction to make silver particle films.[69] Other shapes, including silver prisms which can be made thermally and photochemically[70] and in the form of silver island films, were also reported.[71] While silver nanoparticles are interesting because of their size- and shape-dependent chemical properties, they are also recognized for their antimicrobial activity in fighting infections found in wounds.[72] Using silver-coated materials to prevent infections as an alternative to antibiotics will help combat the rise of antibiotic-resistant bacteria, which are commonly found in post-surgical wounds. [72]

1.6. Our Goals

Our goals in this research are to develop a simple yet effective method for Ge nanoparticle synthesis and to tailor the surface chemistry of Ge nanoparticles.

[vi] Annodization is an electrolytic passivation process. In this example, the substrate (Si) is used as the anode.

Developing comprehensive synthetic methodology, along with an in-depth understanding of each variable in the reaction mechanism—including the process of nucleation of Ge nanoparticles, the interaction between reagents and solvents, the ability to control the size of the Ge nanoparticles, and the way to change the surface chemistry of the Ge—is the backbone of this research. To date most studies emphasize synthesis and report limited surface chemistry tailoring of Ge nanoparticles; furthermore, certain mechanisms have been misreported or poorly understood. An example is the misreporting of the gaseous product evolved during the reduction of GeX_4 (X = Cl, Br, and I).[11] The gaseous product was reported to be H_2, but it was later discovered that the gas evolved could be GeH_4 instead of H_2.[37] There is also a need to develop a more efficient method for nanoparticle purification. One method reported in the literature suggests the use of high-performance liquid chromatography (HPLC) for nanoparticle purification;[11] however, the use of HPLC might not be practical for large-scale production. The type of reducing agent used for the synthesis is also critical because the rate of reduction can change the size of the nanoparticles synthesized. Using a highly reactive reducing reagent, such as NaK_{disp}, and specialized equipment, such as a high-pressure bomb, is impractical and dangerous.[33] The ability to minimize the size distribution of Ge nanoparticles is important since UV-visible data can be collected to understand the absorption properties of Ge nanoparticles. Tanke[34] presented a series of reactions that demonstrates the possibility of tailoring the surface chemistry of germanium with a size distribution of 4 ± 2 nm; however, the broad size distribution of nanoparticles creates difficulty in understanding the broad emission spectra. The surface chemistry and crystallinity of Ge nanoparticles are not often discussed or investigated. Lu *et al.* outlined a new method in Ge nanoparticle synthesis:

using GeI_2 to overcome many disadvantages of using GeI_4;[35] but there is no indication of whether the hydrocarbons were attached to the surface of the nanoparticle. Nanoparticle synthesis by thermolysis, presented by Gerung *et al.*, shows crystalline germanium nanoparticles; however, the Ge nanoparticles have a broad size distribution which limits the Ge nanoparticles' utility.[36]

Based on the reports outlined in previous sections of this chapter, there is a great deal of interest in the synthesis and surface functionalization of Ge nanoparticles. In addition, the ability to control the process of nucleation and the size of the nanoparticles will allow for better characterization and a greater understanding of the Ge nanoparticle and the mechanism of nanoparticle formation. This fundamental research will focus on the development of two different methods in the synthesis of germanium nanoparticles and the tailoring of surface chemistry by hydrogermylation.

We have successfully developed two different synthetic methods that can be used to make hydride-terminated Ge nanoparticles. Ge nanoparticles can be synthesized via metal hydride reduction and high temperature (300°C) reduction of a molecular precursor, GeX_4 (X = Cl, Br, or I), followed by the exploitation of thermally or photochemically initiated hydrogermylation using a terminal alkene. The nanoparticles were characterized using infrared spectroscopy (IR), nuclear magnetic resonance (^{1}H NMR) spectroscopy, ultraviolet visible (UV) spectroscopy, transmission electron microscopy (TEM), x-ray powder diffraction (XRD), and selected area electron diffraction (SAED). The results of our findings are reported and discussed in this thesis.

2. Metal Hydride Reduction of GeX_4 Nanoparticles

2.1. Introduction

The study of nanoparticle clusters composed of ~ 10 to 1000 atoms is of great interest to researchers. Semiconductor nanoparticles, or quantum dots (QD), are known for their size-dependent properties.[73] These properties result from the confinement of charge carriers within a particle that has dimensions smaller than the Bohr radius of an exciton in the bulk material (Chapter 1). Many compound semiconductor quantum dots, such as CdSe, CdS, InP, and GaAs, are known; and methods of preparation afford control over particle size, shape, and surface chemistry.[16,25,74] Quantum confinement in these compound semiconductors is well understood.[75-78] Correspondingly, these direct gap compound semiconductor quantum dots have application in many functional devices, including solar cells, liquid crystals, transistors, and light emitting diodes.[79-82]

Bulk germanium has a narrow indirect band gap (0.67 eV at 291 K).[84] The large Bohr exciton radius (11.5 nm) in Ge makes this semiconductor very attractive because small changes in nanoparticle size should allow for exquisite tuning of the material's photoluminescence (PL) throughout the visible spectrum.[11] Solution-based synthetic procedures applied to the synthesis of compound semiconductor nano-materials often offer simultaneous control of particle shape, size, and surface.[83] Many solution-based procedures have been applied to the synthesis of Ge nanoparticles and have already been summarized in Chapter 1 of this thesis. All known solution methods suffer from significant challenges, including ill-defined surface chemistry, specialized or hazardous precursors, and limited scalability.

This chapter outlines a synthetic protocol that provides a Ge nanoparticle from the metal hydride reduction of a molecular precursor (see Scheme 19) followed by the exploitation of thermally or photochemically initiated hydrogermylation surface reactions to tailor the surface chemistry of the Ge nanoparticle (see Scheme 20).[84]

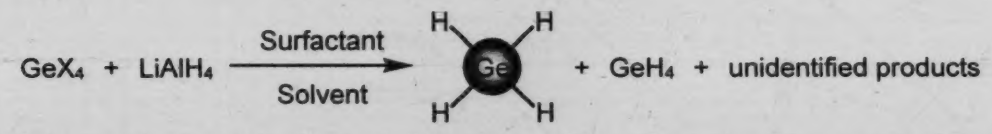

Scheme 19 General scheme that can be used to make germanium nanoparticles from GeX_4 (X = Cl and I). Metal hydride reduction of $GeBr_4$ was not investigated and will not be discussed in this chapter. Surfactants used to limit particle growth included cetyltrimethylammonium bromide (CTAB) and Triton X-100.[84] The unidentified products are the uncharacterized yellow salts present in the solution.

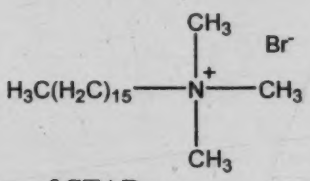

Figure 18 Chemical structure of CTAB.

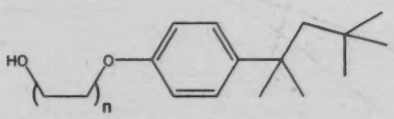

Figure 19 Chemical structure of Triton X-100 (n = 50 – 100).

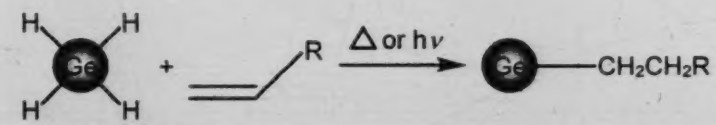

Scheme 20 Reaction scheme for hydrogermylation of Ge nanoparticles. Hydride surface-terminated germanium nanoparticles were heated or exposed to a constant white light source in the presence of excess terminal alkenes, which yielded an alkyl surface-terminated Ge-QD.[84]

2.2. Experimental

2.2.1. Solvents and Reagents

Chloroform (*Merck; EMD Chemicals*) was degassed with argon for 30 minutes before use. Toluene (*Fisher Scientific)*, HPLC-grade pentane (*Caledon Laboratory Chemicals*), methylene chloride (*Fisher Scientific*), and tetrahydrofuran (THF) (*Merck; EMD Chemicals*) were purified by distillation using an Na/benzophenone indicator under an argon atmosphere. Benzophenone (*Fluka; Sigma-Aldrich Co.*) was used for solvent distillation without further purification. Acetonitrile (*Sigma-Aldrich Co.*) was stored in a "sure-seal" bottle under argon.

Deuterated solvents, including chloroform-D (99.8%), benzene-D6 (99.5%), THF-D8 (99.5%), and methanol-D4 (99.8%) (*Cambridge Isotope Laboratories, Inc.*), were used without further purification.

Germanium tetrachloride (*Sigma-Aldrich Co.*) was transferred from an ampule to a grease-free Schlenk flask in an argon-filled glove bag. Germanium tetrabromide (*Sigma-Aldrich Co.*) was stored in a glovebox and used without further purification. Germanium tetraiodide (*Sigma-Aldrich Co.*) was used without further purification.

1-Pentene (*Sigma-Aldrich Co.*) was stored in a sure-seal bottle and used without further purification. 1-dodecene, 1-decene, 1-undecene, and 1-octene (*Sigma-Aldrich Co.*) were used as received.

Triton X–100 (*Applied Science Laboratories Inc.*) and cetyltrimethylammonium bromide (CTAB) (*Sigma-Aldrich Co.*) were used without further purification.

2.2.2. Material Characterization

2.2.2.1. Spectroscopic Characterization

FT-IR spectra were collected using a Nicolet Magna 750 IR spectrometer. Samples were prepared in air and were evaluated as cast films dropped onto KBr cells, or measured in solution using a standard 1 cm solution cell. Air sensitive solution samples were prepared inside a controlled atmosphere drybox. The microscope IR samples were prepared as dry solids, placed on a KBr cell, and measured using a Nicolet Nic-plan FT-IR microscope.

^{1}H NMR spectra were collected on a Varian Inova 300 or 400 MHz spectrometer. Appropriate solvents used to prepare the samples are listed in the caption of the NMR spectrum. NMR samples were prepared inside a controlled atmosphere drybox. The sample solutions were transferred to an NMR tube and temporarily sealed with a septum. After the NMR tube was transferred out of the glovebox, it was frozen in liquid nitrogen and the tube was flame-sealed under vacuum.

Germanium nanoparticles were drop-coated onto an optical-grade quartz cell from a tetrahydrofuran (THF) suspension. The same sample was used to collect UV-visible spectrum data. UV-visible spectra were collected using a HP 8452A diode array spectrophotometer.

2.2.2.2. Electron Microscopy

Transmission electron microscopy micrographs were acquired using a JEOL 2010 transmission electron microscope (TEM) with an accelerating voltage of 200 keV. Carbon-coated, 200-mesh grids used for these analyses were obtained from Structure

Probe Incorporated Supplies. TEM samples were prepared by drop coating the pentane or THF suspension of nanoparticles dropwise onto a grid placed on a piece of Whatman (#2) filter paper and was allowed to dry.

2.2.3. Synthesis of Hydride Surface-Terminated Ge Nanoparticles

All reactions were preformed following strict Schlenk protocol. Using a needle, $LiAlH_4$ or $LiAlD_4$ (0.98 mL, 0.1 M in THF, 0.98 mmol) was introduced into a dry Schlenk flask containing $GeX_{4(s)}$ (0.50 g of GeI_4 or 0.18 g of $GeCl_4$, 0.862 mmol), surfactant (*e.g.*, 0.024 g of CTAB, 0.0658 mmol; or 1 mL of Triton X-100), and dry toluene (or pentane). The solution was allowed to stir for 10 minutes as the color gradually changed from dark red to dark yellow to light yellow to golden yellow. Hydride-terminated Ge nanoparticles were never isolated from this reaction mixture due to extreme air sensitivity; however, a small sample of crude product (**1**, X = I; **2**, X = Cl) obtained from this reaction mixture was evaluated using FT-IR, UV-visible spectroscopy, and TEM.

2.2.4. Extraction of Alkyl Surface-Terminated Ge Nanoparticles from (**1**) via Hydrogermylation

An excess of terminal alkene (*e.g.*, 2.0 mL, 9.72 mmol of 1-undecene) was added to the crude reaction mixture prepared following the procedure outlined in Section 2.3. The surface termination reaction was initiated thermochemically or photochemically.

Thermochemical-Initiated Surface Termination

The mixture was refluxed in an inert atmosphere with subdued light for 2 hours and allowed to cool to room temperature. Upon standing, a yellow precipitate settled out, leaving a faint yellow supernatant.

Photochemical-Initiated Surface Termination

The mixture was stored in an inert atmosphere and exposed to a white light source (60 W light bulb) for 24 hours at room temperature. Upon standing, a yellow precipitate settled out, leaving a faint yellow supernatant.

The supernatant from the thermal- or photo-initiated functionalization reaction was transferred by canula to a clean, dry Schlenk flask. The remaining solids were "washed" three times with toluene (or pentane) and placed in an ultrasonic bath. After the yellow precipitates settled out, the "washed" supernatant was collected and transferred to the Schlenk flask containing the original reaction supernatant solution. The solvent was subsequently removed and evaporated to dryness to yield a yellow oily residue. The residue was triturated[viii] with diethyl ether to yield a waxy yellow solid that was further washed three times with pentane followed by three washes with ethanol, then evaporated dry. Waxy solids were obtained from thermochemical-initiated hydrogermylation reactions using 1-decene (**3a**), 1-undecene (**3b**), and 1-dodecene (**3c**), and from photochemical-initiated reactions using 1-pentene (**4a**) and 1-dodecene (**4b**). The waxy solids were characterized using FT-IR, ^{1}H NMR, UV-visible spectroscopy, and TEM.

[viii] Trituration is the process of turning a substance into a fine powder.

2.3. Results and Discussion

2.3.1. Fourier Transform Infrared Spectroscopy

FT-IR spectroscopy was used to probe particle surface chemistry. A representative FT-IR spectrum of crude hydride-terminated Ge nanoparticles, prepared from $GeCl_4$ and GeI_4 precursors (**1**) and (**2**), is shown in Figure 20. The Ge-H stretching (ν_{Ge-H}) absorption is clearly present at 2067cm^{-1}. This observation is consistent with the crude reaction mixture containing hydride-terminated germanium.[30,84,85] Replacement of $LiAlH_4$ (**1a**) with $LiAlD_4$ (**1b**) results in the expected isotopic shift of Ge-D stretch to 1455 cm^{-1}. This observation further supports that the Ge nanoparticle surface is hydride (deuteride) terminated. Clearly, these spectra are dominated by characteristic absorptions of the surfactant matrix; thus, no further assignments were made. IR absorptions of (**1a**), (**1b**), and (**2**) are tabulated in Table 1.

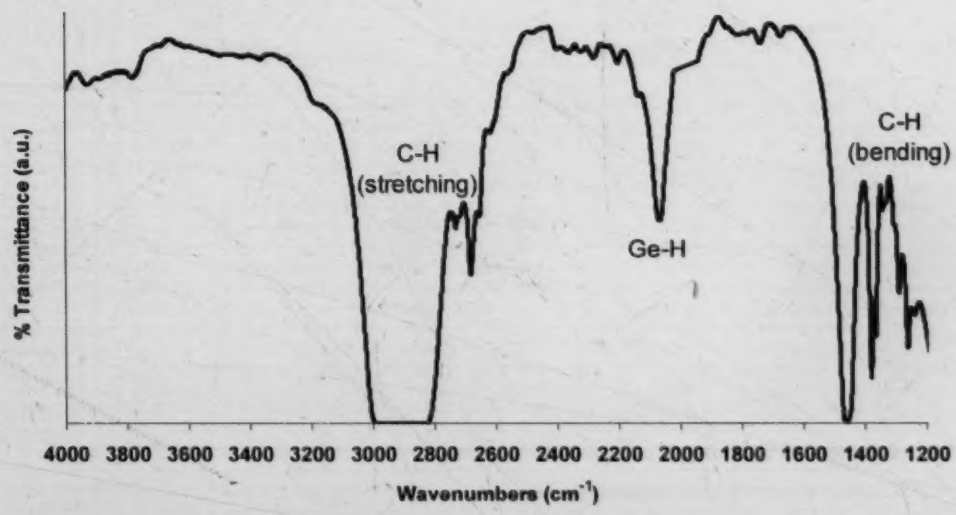

Figure 20 FT-IR of crude reaction mixture of (**2**) showing ν_{Ge-H} stretching at 2067 cm^{-1}.

Table 1 FT-IR data for hydride terminated Ge nanoparticles samples.

Precursor	Absorption wavenumbers (cm^{-1})
1a	2916 cm^{-1} (m, s, C-H sp^3 stretching), 2067 cm^{-1} (m, s, Ge-H stretching)
1b	3053 cm^{-1} (m, s, C-H sp^2 stretching), 2960 cm^{-1} (s, s, C-H sp^3 stretching), 2872 cm^{-1} (m, s, C-H sp^3 stretching), 1458 cm^{-1} (m, s, Ge-D stretching)
2	3054 cm^{-1} (s, s, C-H sp^2 stretching), 2980 cm^{-1} (s, s, C-H sp^3 stretching), 2067 cm^{-1} (m, s, Ge-H stretching), 1471 cm^{-1} (s, s, C-H bending)

A representative FT-IR spectrum of Ge nanoparticles having undergone photochemical-initiated hydrogermylation with 1-dodecene and 1-pentene is shown in Figure 21. The absence of a broad peak at 2067 cm^{-1} (ν_{Ge-H}) found in hydride-terminated Ge nanoparticles (**1a**) and (**2**) suggests that hydrogermylation of the Ge nanoparticles had taken place. This procedure effectively replaces hydride termination sites with alkyl groups via hydrogermylation. The aliphatic stretching ν_{C-H} (sp^3) at 2974 cm^{-1} and 2859 cm^{-1} present in both spectra indicate that alkyl groups are present. The presence of Ge-C vibrations at 850 cm^{-1} (ν_{Ge-C}) formed between the alkyl chain and the Ge nanoparticle surface further supports that surface functionalization had taken place. The presence of weak absorption peaks in the fingerprint region (ν_{Ge-O} 870 to 910 cm^{-1}) indicates that Ge might also be coated with an oxide surface.[86]

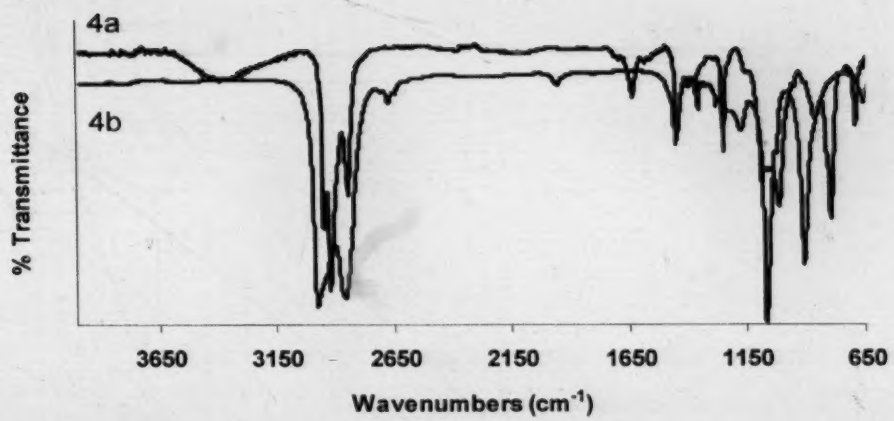

Figure 21 IR spectra of Ge-QD synthesized using $GeCl_4$ and functionalized with 1-pentene (**4a**) and 1-dodecene (**4b**) by photochemical-initiated hydrogermylation.

Table 2 FT-IR data for alkyl-terminated Ge nanoparticles.

Compound	Absorption wavenumbers (cm^{-1})
3a	2850 cm^{-1} (s, s, C-H sp^3 stretching), 1460 cm^{-1} (m, s, C-H bending), 1261 cm^{-1} (s, s, C-H bending), 876 cm^{-1} (w, s, Ge-O stretching)
3b	3400 cm^{-1} (w, b, O-H stretching), 2922 cm^{-1} (s, s, C-H sp^3 stretching), 2850 cm^{-1} (s, s, C-H sp^3 stretching), 1460 cm^{-1} (w, s, C-H sp^2 bending), 850 cm^{-1} (m, b, Ge-C stretching)
3c	2981 cm^{-1} (s, s, C-H sp^3 stretching), 2870 cm^{-1} (s, s, C-H sp^3 stretching), 1463 cm^{-1} (s, s, C-H bending), 806 cm^{-1} (w, s, Ge-O stretching)
4a	3400 cm^{-1} (w, b, O-H stretching), 2956 cm^{-1} (s, s, C-H sp^3 stretching), 2923 cm^{-1} (s, s C-H sp^3 stretching), 2854 cm^{-1} (s, s, C-H sp^3 stretching), 1648 cm^{-1} (w, s, C=C stretching), 1457 cm^{-1} (w, s, C-H bending), 911 cm^{-1} (w, s, Ge-O stretching)
4b	2974 cm^{-1} (s, s, C-H sp^3 stretching), 2859 cm^{-1} (s, s, C-H sp^3 stretching), 1959 cm^{-1} (w, s, Ge-H stretching – trace), 1459 cm^{-1} (m, s, C-H bending), 1180 cm^{-1} (m, s, C-H bending)

2.3.2. ^{1}H Nuclear Magnetic Resonance Spectroscopy

^{1}H NMR spectroscopy further supports the conclusions drawn from IR analysis confirming hydrogermylation took place.[31] Nanoparticles synthesized using different Ge halide precursors GeX_4 (X = Cl, and I) and functionalized with terminal alkenes were

investigated. A representative spectrum is shown in Figure 22 and ^{1}H NMR analysis of **3a, 3b, 3c, 4a,** and **4b** are tabulated in Table 3. The NMR samples for the nanoparticles synthesized using different precursors were prepared following the same procedure. Each of the samples was placed under vacuum for 24 hours to ensure removal of all solvents prior to NMR sample preparation.

The peaks in a ^{1}H NMR spectrum of Ge nanoparticle samples **3a, 3b, 3c, 4a,** and **4b** were broad.[34] This phenomenon has been attributed to nanoparticles tumbling in solution at a slower timescale which in turn will broaden up the peaks observed in the ^{1}H NMR spectra.[85] The rate of tumbling is also dependent on the features on the surface of the Ge nanoparticle.[35] The surface chemistry of the Ge nanoparticle, specifically the length of the alkyl chain, has an impact on the broadening of peaks on the ^{1}H NMR spectra. The spectra of a Ge nanoparticle hydrogermylated with a shorter alkyl chain (*e.g.*, decane) were found to have broader peaks compared to Ge nanoparticles terminated with longer alkyl chains (*e.g.*, dodecene). The broader peaks are usually observed at the upfield region where the methyl ($R\text{-}CH_3$) or ethyl ($R_2\text{-}CH_2$) chemical shifts. It was suggested that the protons that are closer to the core of the Ge nanoparticle might tumble more slowly than the protons that are furthest away from the core which would rotate as if the proton exists free in solution.[33,87] When long alkyl chains were functionalized onto the Ge nanoparticles (**3b**, **3c**, and **4b**), sharper peaks were observed at the upfield region (see Table 3). The presence of sharp peaks indicates that the protons on the carbon that are closer to the core of the Ge nanoparticle might be tumbling slower than the protons on the carbon that is furthest away.

The NMR samples collected from photo-initiated hydrogermylation show fewer impurities compared to NMR samples collected from thermal-initiated hydrogermylation. It can be postulated that photochemical-initiated hydrogermylation can provide a more complete functionalization compared to thermal-initiated hydrogermylation. It should be noted that both the photochemical- and thermal-initiated Ge nanoparticles were prepared following the same procedure.

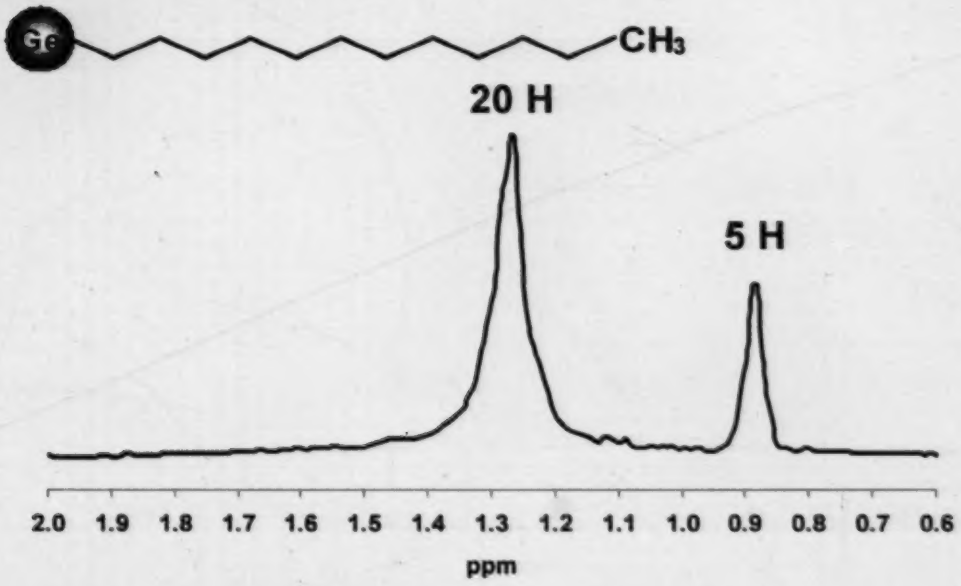

Figure 22 ^{1}H NMR spectra of Ge nanoparticle that had undergone hydrogermylation with 1-dodecene (**3c**).

Table 3 ^{1}H NMR data for alkyl-terminated Ge nanoparticles samples.

Compound	Solvent	δ (ppm)
3a	C_6D_6	0.252 (s, 2H, R-CH_2), 0.859 (m, 3H, R-CH_3), 1.228 (m, 16H, R-CH_2)
3b	C_6D_6	0.925 (m, 3H, R-CH_3), 1.305 and 1.413 (m, 16H, R-CH_2), 3.565 (s, 4 H, R-CH_2)
3c	C_6D_6	0.868 (m, 5H, R-CH_3, R-CH_2), 1.270 (m, 20H, R-CH_2)
4a	d-THF	0.890 (m, 3H, R-CH_3), 1.182 (m, 8H, R-CH_2)
4b	d-THF	0.895 (t, 3H, R-CH_3), 1.735 (s, 22H, R-CH_2)

2.3.3. Transmission Electron Microscopy

A typical bright field transmission electron micrograph of Ge nanoparticles (**2**) is shown in Figure 23. Complicating factors, including extreme atmospheric sensitivity of the Ge-QD, hindered the acquisition of a meaningful size distribution data. Still, we estimate that typical hydride-terminated Ge nanoparticles are approximately 3 nm in diameter (**3d**).

Figure 23 Transmission electron micrographs of ~ 3 nm Ge-QD (**3d**). The bar on the transmission electron micrographs represents 20 nm.

A representative bright field transmission electron micrograph obtained for alkyl surface-functionalized Ge nanoparticles synthesized using GeI_4 (**3d**) is shown in Figure 24. Like in other studies, particles tend to aggregate suggesting uniform surface functionalization.[88] The diameter of the germanium nanoparticles was determined by measuring 408 particles from different regions of the grid (see Figure 24). The average particle size was determined to be 5 nm, and 88% of the particles have sizes within the range of 2 to 10 nm. The limited TEM contrast between the carbon-coated grid and the Ge particles also hindered the acquisition of meaningful size distribution data. There were also some large agglomerations of particles (~ 18 nm) that were randomly scattered throughout the grid.

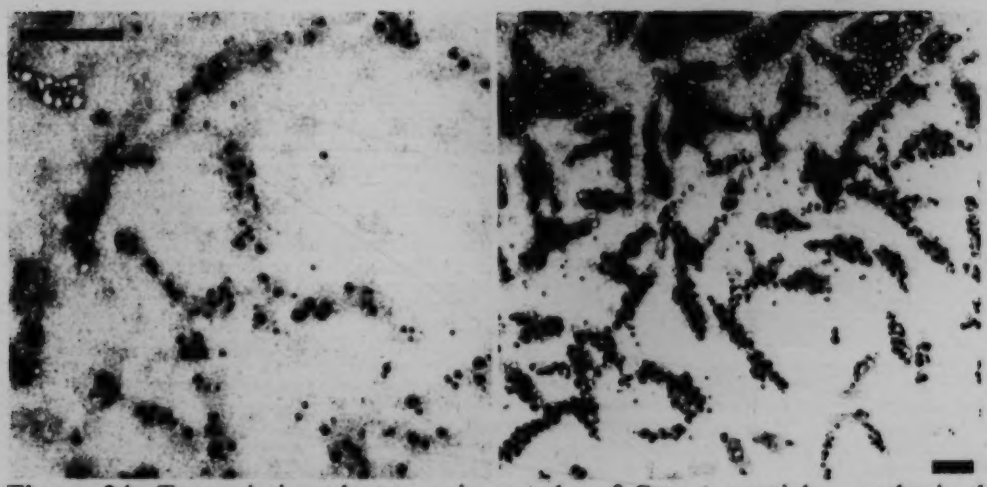

Figure 24 Transmission electron micrographs of Ge nanoparticles synthesized using GeI_4 and terminated with undecane (**3b**). The size of the nanoparticles averaged 5 nm and ranged from 2 to 10 nm. The bar on each Transmission electron micrographs represents 100 nm.

The diameter of the Ge nanoparticles is polydispersed with a range of 2 to 10 nm (see Figure 25). A Gaussian distribution was not observed in the size distribution; instead, the size distribution suggests that diameters of 3, 5, and 9 nm were dominant in this sample. The presence of larger nanoparticles suggests that the process of hydrogermylation can lead to an increase in diameter of Ge nanoparticles; furthermore, it suggests that Ostward ripening[ix] had occurred during hydrogermylation.

[ix] Ostward Ripening is the nucleation (growth) of larger particles at the expense of smaller particles.

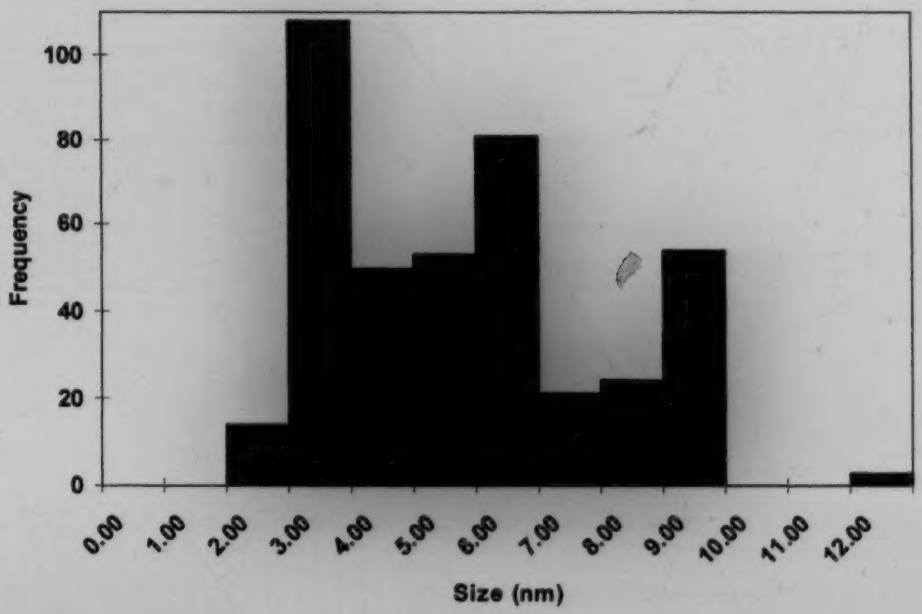

Figure 25 The sizes of Ge nanoparticles synthesized using GeI_4 and terminated with undecane (**3b**) were determined by measuring a total of 408 particles from different regions of the TEM grid. The average diameter of the nanoparticles was 5 nm with a range from 2 to 10 nm.

2.3.4. Selected Area Electron Diffraction

The selected area electron diffraction (SAED) of the Ge nanoparticles (**3d**), synthesized using GeI_4 as a precursor, was examined (see Figure 26). The SAED of the Ge nanoparticle sample shows five rings that are readily indexed to (111), (220), (311), (331), and (440).[84] An x-ray powder diffraction (XRD) spectrum of bulk Ge was collected, and the peaks on the XRD were indexed to (111), (220), (311), (331), (333), (400), (422), (440), and (531). The XRD of bulk Ge and SAED data suggests that Ge nanoparticles and bulk Ge have the same lattice spacings.

Figure 26 Selected electron diffraction of Ge nanoparticles synthesized using GeI_4 and terminated with undecane (**3b**). The pattern is indexed as (111), (220), (311), (331), and (440) lattice spacing of Ge.

2.3.5. Ultraviolet Visible Spectroscopy

Data from UV-visible spectroscopy provide insight into the electronic structure of nanoparticles. Acquiring the UV-visible spectra was difficult because the nanoparticles were inside an oily matrix made of surfactants and other contaminants (*e.g.*, I_2). An example of a typical UV-visible spectrum (see Figure 27) and a summary of features found in UV-visible spectra of the Ge samples synthesized are tabulated below (see Table 4). These features were compared to bulk Ge and Ge nanoparticles (d = 4.0 nm) synthesized using an alternative method.[11] The UV-visible spectrum of bulk Ge shows an absorption at 288 nm and a shoulder at ~ 550 nm which was believed to correspond to the direct Γ_{25} to Γ_{15} transition at L (2.1 eV) and X (4.3 eV) respectively (see second figure in Figure 4).[11] The UV-visible spectrum of Ge nanoparticles (d = 4.0 nm) reported

from literature also shows two absorption peaks at 300 and 355 nm which corresponds to the direct Γ_{25} to Γ_{15} transition at Γ (3.4 eV).[1] The optical absorption peaks of the nanoparticles, synthesized using the method described in Sections 2.2.3 and 2.2.4, were analyzed. The 322 nm (**1** and **2**), 358 nm (**4a**), and 370 nm (**4b**) peaks most likely represent the direct Γ_{25} to Γ_{15} transition at Γ (3.4 eV). It is believed that a weak (0.1 eV to 0.4 eV) quantum confinement effect was present at this lower transition. The 276 nm (**3c**), 278 nm (**2**), 289 nm (**4a**), 297 nm (**4b**), and 300 nm (**3c**) peaks most likely represent the direct Γ_{25} to Γ_{15} transition at X (4.3 eV). It is believed that a weak (0.1 eV to 0.3 eV) quantum confinement effect was present at this higher transition.

The data collected from our UV-visible spectrum suggest that the effects of quantum confinement are present and that energy transitions, which normally do not occur in bulk Ge, are observed in the Ge nanoparticles as the effects become more apparent when the diameter of Ge nanoparticles becomes less than the Bohr radius. Our hydrogen-terminated and alkyl-terminated Ge nanoparticles were 3 nm and ca. 5 nm respectively which is less than the Bohr radius of Ge. The direct Γ_{25} to Γ_{15} transition at X was observed in both bulk Ge and Ge nanoparticles whereas the transition at Γ was only observed in Ge nanoparticles. The absorbance at 278 nm which corresponds to the transition at Γ suggests that quantum confinement is apparent in our nanoparticle.

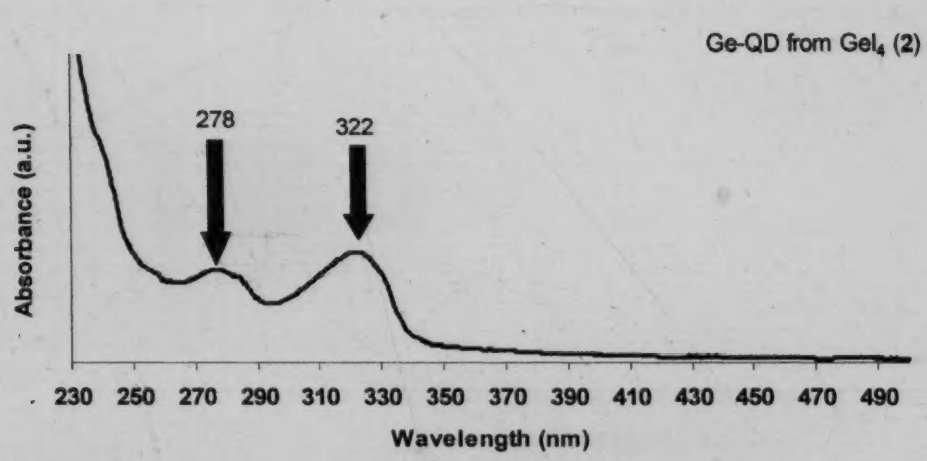

Figure 27 UV-visible spectra of Ge-QD synthesized using GeI_4.

Table 4 Optical absorption wavelength of different Ge nanoparticle samples.

Precursor	Optical Absorptions in wavelength (nm & eV)
Bulk Ge[11]	Absorption at 288 nm (4.3 eV) and shoulder at ~ 550 nm (2.2 eV)
Ge nanoparticles (d = 4.0 nm)[11]	Absorption at 300 nm (4.1 eV) and 355 nm (3.5 eV), and shoulder at ~ 550 nm (2.2 eV)
1	Absorption at 278 nm (4.5 eV) and 322 nm (3.8 eV)
2	Absorption at 278 nm (4.5 eV) and 322 nm (3.8 eV)
3a	Absorption at 278 nm (4.5 eV)
3b	UV-visible spectra were not acquired
3c	Absorption at 276 nm (4.5 eV) and 300 nm (4.1 eV)
4a	Absorption at 289 nm (4.3 eV) and 358 nm (3.5 eV)
4b	Absorption at 297 nm (4.2 eV) and 370 nm (3.3 eV)

2.4. Conclusion

The methodology in preparing hydride-terminated Ge nanoparticles was discussed. Hydride-terminated germanium nanoparticles can be prepared by metal hydride reduction of GeX_4 (X = Cl, and I) using $LiAlH_4$ in the presence of surfactants (Triton X-100 or CTAB). The two different halides were investigated to see if crystallinity of the Ge nanoparticles can be exploited by changing the halogens of the Ge source. Limited characterization of the hydride-surfaced Ge nanoparticles was performed

using FT-IR and TEM. The hydride surface was confirmed by the the presence of ν(Ge-H) stretching using FT-IR spectroscopy. An isotopic shift of ν(Ge-D) at 1458 cm^{-1} was observed when $LiAlD_4$ was used instead of $LiAlH_4$. Transmission electron micrographs support the size of the nanoparticles to be 3 nm in diameter.

The methodology in tailoring the surface chemistry of germanium nanoparticles via hydrogermylation was also investigated. Hydrogermylation can be initiated thermally and photochemically in the presence of a terminal alkene. The resulting functionalized products were characterized. The absence of ν(Ge-H) stretching and vinyl group with the appearance of alkyl absorptions ν(Ge-C) and ν(C-H) confirmed the surface of the Ge nanoparticle had undergone hydrogermylation. The ^1H NMR spectrum of Ge nanoparticles shows no evidence of vinyl groups present in the sample. The average size of the nanoparticles was determined to be 5 nm with a range between 2 and 10 nm; particles with diameters as large as 18 nm were observed. The UV visible spectrum showed the presence of two absorptions at the direct Γ_{25} to Γ_{15} transition at Γ and X orientation. The selected area diffraction pattern indicates the particles made using GeI_4 and bulk Ge have the same lattice spacings thus the Ge nanoparticles process the diamond lattice Ge structure

3. High Temperature Reduction of GeX_4

3.1. Introduction

This chapter discusses an alternative method for the synthesis of germanium nanoparticles by thermal reduction.[18,36] Thermal reduction offers direct and single source solution synthesis of nanoparticles without the need for additional solvent (*i.e.*, the surfactant was used as the solvent for these reactions). The use of high temperature can overcome the limited precursor reactivity.[35] Furthermore, the rate of precursor degradation and the rate of nucleation can be controlled more effectively by changing the reaction temperature. By selecting the proper reaction temperature and using coordinating solvents and surfactants, the size of the nanoparticles and the growth mechanism can be effectively controlled.[35]

This chapter outlines an alternative synthetic protocol that provides germanium quantum dots through high temperature reduction of GeX_4 (X = Cl, Br, and I) (see Scheme 21) followed by the exploitation of a hydrogermylation[84] surface reaction (see Scheme 22). The hydrogermylation surface reaction was explained in more detail in Chapter 2.

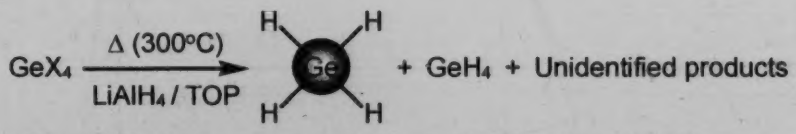

Scheme 21 High temperature reduction of GeX_4 to yield Ge nanoparticles. $LiAlH_4$ is added to a 300°C mixture of germanium precursor GeX_4 (X = Cl, Br, or I) dissolved in trioctylphosphine (TOP) (see Figure 28).

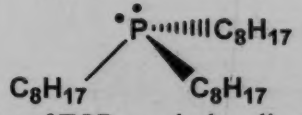

Figure 28 The structure of TOP, a colorless liquid surfactant.

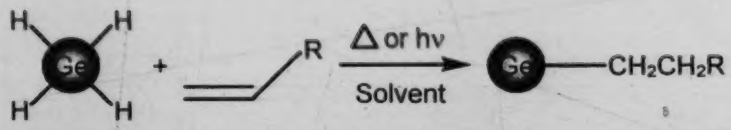

Scheme 22 The reaction scheme for hydrogermylation of Ge-NP. Hydrogen surface-terminated germanium nanoparticles from Scheme 21 are heated with excess terminal alkenes. 1-pentene was routinely used to terminate the surface of Ge-QD.

3.2. Experimental

3.2.1. Reagents

Chloroform (*Merck; EMD Chemicals*) was degassed with argon for 30 minutes before use. Toluene (*Fisher Scientific)*, HPLC-grade pentane (*Caledon Laboratory Chemicals*), methylene chloride (*Fisher Scientific*), and tetrahydrofuran (THF) (*Merck; EMD Chemicals*) were purified by distillation using a Na/benzophenone indicator under an argon atmosphere. Benzophenone (*Fluka; Sigma-Aldrich Co.*) was used for solvent distillation without further purification. Acetonitrile (*Sigma-Aldrich Co.*) was stored in a "sure-seal" bottle under argon.

A Pure-Solv solvent purification system (PS-400s) (*Innovative Technology*) was used to purify the optima-grade solvents THF, toluene, and methanol (*Fisher Scientific*). Spectrophotometric-grade and inhibitor-free (99%) diethyl ether (*Sigma-Aldrich Co.*) was used for the solvent purification system. Certified-grade pentane (*Fisher Scientific*) was used in the Pure-Solv system.

Deuterated solvents, including chloroform-D (99.8%) and methanol-D_4 (99.8%) (*Cambridge Isotope Laboratories, Inc.*), were used without further purification.

Germanium tetrachloride (*Sigma-Aldrich Co.*) was transferred from an ampule to a Schlenk flask in an argon-filled glovebag. Germanium tetrabromide (*Sigma-Aldrich*

Co.) was stored in a glovebox and used without further purification. Germanium tetraiodide (*Sigma-Aldrich Co.*) was used without further purification.

1-Pentene (90%) (*Sigma-Aldrich Co.*) was stored in a sure-seal bottle and used without further purification.

Trioctylphosphine (TOP) (*Sigma-Aldrich Co.*) and Sephadex-G50 (*Sigma-Aldrich Co.*) were used without further purification.

3.2.2. Material Characterization

3.2.2.1. Spectroscopy Characterization

The IR and ^{1}H NMR data were collected following procedures outlined in Section 2.2.2.1 in Chapter 2.

X-ray diffraction patterns were measured using an Inel diffractometer equipped with a CPS 120 detector with a CuK_α source. Samples were ground using a mortar and pestle. The resulting uniform powder was mounted on an Al sample holder, and the diffraction data were acquired for 14 hours in air.

3.2.2.2. Electron Microscopy

Transmission electron micrographs were acquired using a JEOL 2010 transmission electron microscope (TEM) with an accelerating voltage of 200 keV. The carbon-coated, 200-mesh grids used for this analysis were obtained from Structure Probe Incorporated supplies. TEM samples were prepared by drop coating a copper grid placed on filter paper with nanoparticle solutions in either pentane or THF.

3.2.3. Synthesis of Hydride Surface-Terminated Ge Nanoparticles

$LiAlH_4$ (5.5 mL, 1 M THF, 5.5 mmol) was transferred to a Schlenk flask filled with TOP (5 mL, 11.2 mmol). The flask was placed under vacuum overnight to facilitate the removal of THF and the suspension of the $LiAlH_4$ in the TOP. In an argon-filled drybox, GeX_4 (X = Cl, Br, I; 1.38 mmols) was transferred to a Schlenk flask and sealed with a septum. TOP (5 mL, 11.2 mmol) was added to the Schlenk flask containing GeX_4 after it was removed from the box. The mixture containing the GeX_4 was stirred and warmed to 120°C using a sand bath, then moved to another sand bath preheated to 300°C and allowed to equilibrate. The mixture of TOP and $LiAlH_4$ was transferred into the Schlenk flask, and the mixture was left in the 300°C sand bath for 1 hour, and then allowed to cool to room temperature. The Ge nanoparticles synthesized using $GeCl_4$ (**5a**), $GeBr_4$ (**5b**), and GeI_4 (**5c**) precursors were characterized using FT-IR, XPS, and TEM, and were used without further purification or characterization.

3.2.4. *n*-alkyl Surface Termation of **5a**, **5b**, and **5c**

A reflux apparatus was assembled on the reaction flask and purged with argon. 1-Pentene (6.5 mL, 0.059 mol) was added into the reaction mixture following Scheme 21. The mixture was refluxed for 4 hours, and its contents were placed under vacuum to remove any volatile impurities while cooling to room temperature.

Using a canula, the TOP layer was transferred to a new round Schlenk flask and put aside. The solids were "washed" with chloroform and placed in an ultrasonic bath for 5 minutes. The mixture was centrifuged for 15 minutes and the supernatant removed. The waxy solid fractions were collected and resuspended with sonication in 20 mL of

chloroform. The mixture was filtered through a fritted column filled with 1.5 cm of Sephadex-G50. The filtrate was collected and allowed to sit under argon brown solids to precipitate out of the solution. Solids were isolated upon centrifugation for 15 minutes. The colorless supernatant was discarded; the solids made using $GeCl_4$ (**6a**), $GeBr_4$ (**6b**), and GeI_4 (**6c**) were dried in a vacuum and characterized by IR, ^1H NMR, XPS, TEM and EDX.

3.3. Results and Discussion

Germanium nanoparticles were prepared via the high temperature lithium aluminium hydride reduction of germanium tetrahalides (*i.e.*, $GeCl_4$, $GeBr_4$, and GeI_4) in surfactant solutions. Following reaction with 1-pentene, a brown/black precipitate was formed. The resulting product was isolated using a centrifuge and evaluated using techniques outlined in Section 3.2.4.

3.3.1. Transmission Electron Microscopy

A typical bright field TEM image is shown in Figure 29. Like other reports, we observe that particles tend to aggregate, which suggests uniform surface functionalization.[88] In addition, particles appear to be encapsulated in a non-crystalline matrix, which is proposed to be amorphous germanium (based upon the XRD analysis [*vide infra*]). These complicating factors, as well as the limited TEM contrast between the carbon-coated grid and the Ge particles, hindered acquisition of meaningful size distribution data. Nevertheless, we estimate the particle dimensions to be approximately

3.0, 1.2, and 5.8 nm for products obtained from the reduction of the $GeCl_4$, $GeBr_4$, and GeI_4 respectively. A summary of the Ge nanoparticle dimensions is in Table 5.

Figure 29 Transmission electron micrograph of Ge nanoparticles (black dots) synthesized using GeI_4 with an average particle size of 5.8 nm (n = 78).

Table 5 TEM data for Ge nanoparticles samples.

Compound	Size distributions on Transmission Electron Micrographs
5a	Particle size of 1.5 to 3 nm
5b	Particle size of 1.2 nm
5c	Particle size of 3.2 to 5.8 nm
6a	TEM not acquired
6b	Particle size of 1.2 nm
6c	Particle size of 15.1 nm

3.3.2. Energy-Dispersive X-Ray Spectroscopy

EDX indicates that the reaction products are made up of Ge with trace amounts of impurities from reagents (Al, O, P, and C) and the sample grid (C, Cu, and Fe) (see Figure 30). Note that the intensity of the peaks shown on the EDX cannot be used to determine the concentration of impurities because the instrument was calibrated to detect elemental species only.

Ge was not detected in **6a** which could be because Ge nanoparticles were not present in the section of the grid that was investigated or because an insufficient concentration of Ge nanoparticles was drop-coated onto the grid. The EDX data of other compounds are in Table 6.[90]

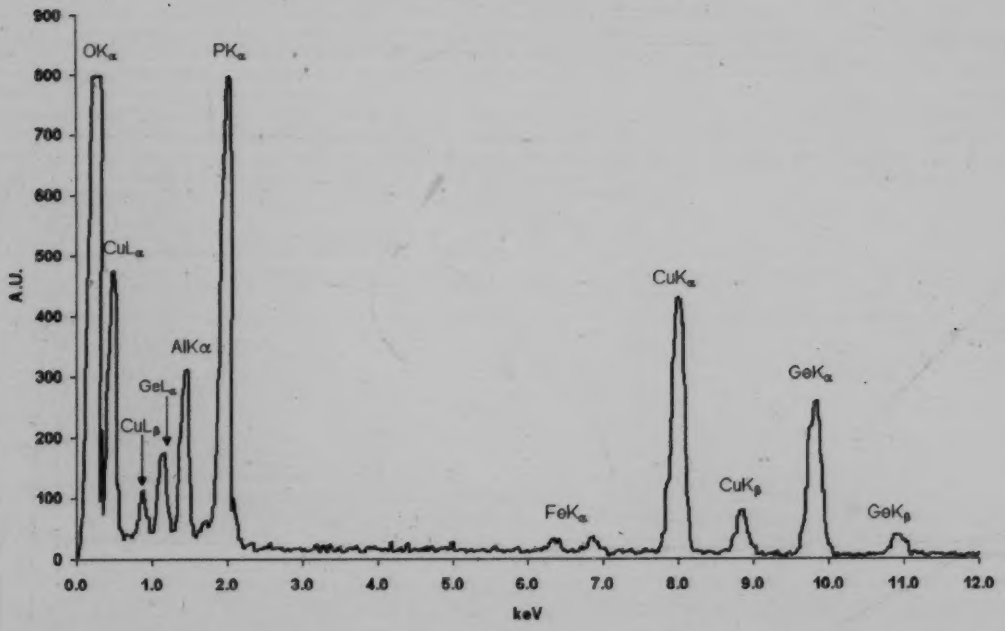

Figure 30 EDX analysis of Ge nanoparticles synthesized using GeI_4 indicates the presence of multiple elements.

Table 6 EDX data for Ge nanoparticles samples.

Compound	X-rays detected
5a	OK_α, CuL_α, AlK_α, SiK_α, PK_α, CuK_α, CuK_β, GeK_α, GeK_β
5b	OK_α, CuL_α, $GeL_{\alpha 1}$, AlK_α, SiK_α, PK_α, CuK_α, CuK_β, GeK_α, GeK_β
5c	CK_α, OK_α, CuL_α, CuL_β, GeL_α, AlK_α, PK_α, FeK_α, CuK_α, CuK_β, GeK_α, GeK_β
6a	CK_α, OK_α, SiK_α, PK_α, CuK_α
6b	OK_α, CuL_α, $GeL_{\alpha 1}$, AlK_α, PK_α, CuK_α, GeK_α
6c	CK_α, OK_α, $CuL_{\alpha 1}$, $GeL_{\alpha 1}$, AlK_α, SiK_α, PK_α, SK_α, ClK_α, CuK_α, CuK_β, GeK_α

3.3.3. X-ray Powder Diffraction

X-ray powder diffraction of hydride- and pentane-terminated Ge nanoparticles show evidence of amorphous Ge in all samples (see Figures 31 and 32) as evidenced by two broad peaks at approximately 28° and 50° 2θ.[90] Previous studies have shown that

the onset of crystallization occurs upon annealing Ge nanoparticles at approximately 600°C.[90] Because the nanoparticles synthesized in this chapter were heated to only 300°C, it is understandable that the nanoparticles exhibit amorphous behaviour when analyzed using XRD and TEM. To observe higher crystalline Ge nanoparticles, it might be necessary to heat up the reaction mixture above 600°C.

Sharp peaks were observed only in the XRD generated from hydride-terminated Ge nanoparticles prepared using $GeCl_4$ (**5a**) (see Figure 36). The sharp peaks were indexed to (111), (220), (311), (331), (333), (400), and (422). The peaks of an XRD of bulk Ge were indexed to (111), (220), (311), (331), (333), (400), (422), (440), and (531). The reflections on both XRDs are equivalent, which suggests that the hydride-terminated Ge nanoparticles synthesized using $GeCl_4$ possess the diamond lattice Ge structure.

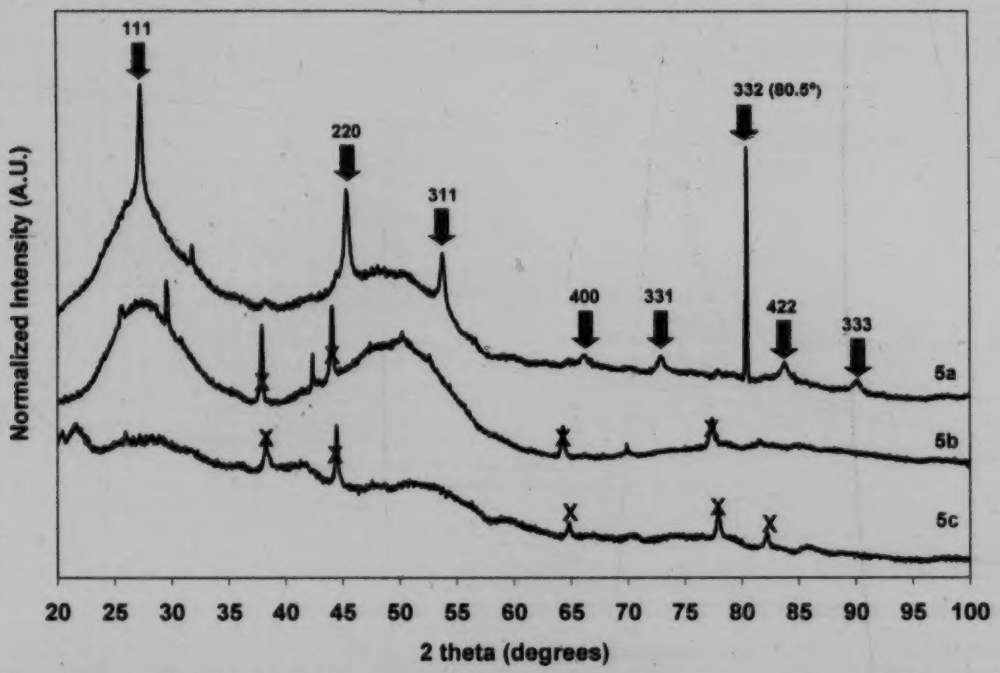

Figure 31 XRD of the black powder product collected before hydrogermylation (**5a**, **5b**, and **5c**). The surface of the Ge nanoparticle is hydride terminated. The peaks with black arrows correspond to the peaks found in Ge powder. The peak highlighted with a black arrow is from an uncharacterized impurity. The peaks marked "X" are peaks from the Al sample holder.

Table 7 XRD data for Ge nanoparticles analyzed prior to hydrogermylation.

Compound	Reflected angle and corresponding Miller indicies: 2θ (hkl)
5a	27.4° (111), 45.4 ° (220), 53.8 ° (311), 66.2° (400), 72.9 ° (311), 83.8 ° (422), 90.2 ° (333)
Bulk Ge	27.2° (111), 45.3° (220), 53.7° (311), 66.0° (331), 72.9° (331), 83.7° (422), 90.1° (333), 100.8° (440), 107.2° (531)

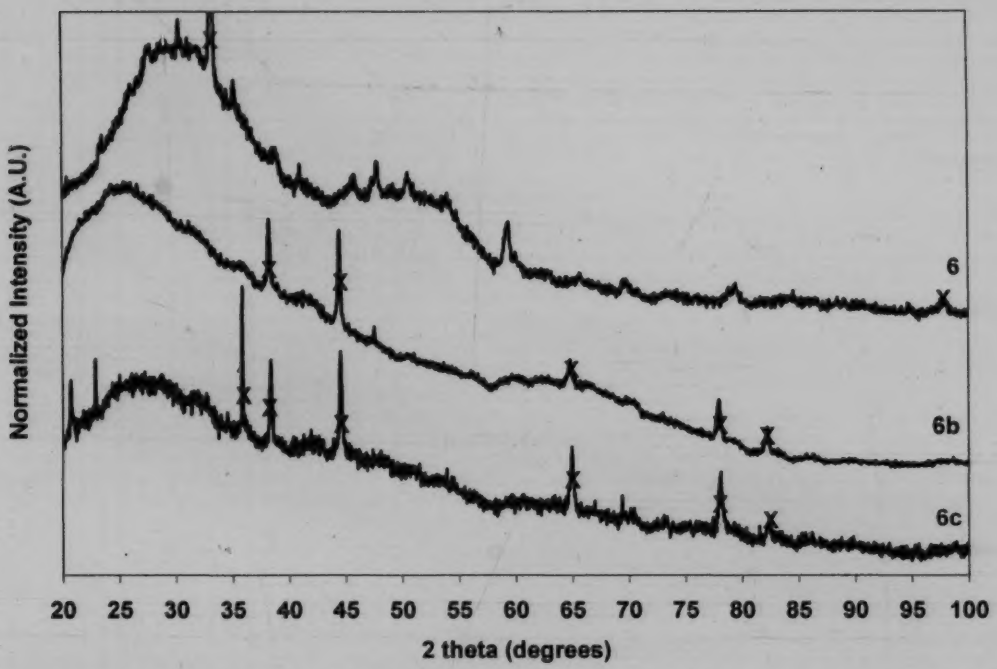

Figure 32 XRD of the black powder product collected after being terminated with pentane (**6a**, **6b**, and **6c**). The peaks marked "X" are peaks from the Al sample holder.

The Scherrer equation (see Figure 33) was used to estimate the diameter of the hydride-terminated Ge (**5a**) because trace crystalline Ge was observed on the XRD. The Scherrer analysis method assumes crystalline particles are present in the sample. The results of the Scherrer analysis for all the reflections from the XRD of **5a** are tabulated in Table 8. Based on the Scherrer equation, the estimated diameter of the Ge nanoparticles ranged from 15.0 to 28.8 nm. This estimate does not agree with TEM: the size of Ge nanoparticles on TEM ranged from 1.5 to 3.0 nm. This may be understood in the context that XRD is dominated by the largest particles present.

$$D = \frac{K\,\lambda}{B_p \cos\theta_B}$$

Figure 33 Scherrer equation was used to estimate the diameter (D) of the Ge nanoparticles. K is the shape factor which has a value of 0.9. λ is the wavelength of the x-ray radiation (1.54056Å). B_p is the broadening of the peak at full width at half maximum (FWHM) (in radians). θ_B is the Bragg angle at half width.

Table 8 Scherrer analysis of all the reflections from XRD of **5a**.

Bragg angle (θ)	Reflections on XRD	B_p (FWHM) (2θ)	Estimated diameter (nm)
27.4	(111)	0.34	23.8
45.4	(220)	0.37	23.0
53.8	(311)	0.31	28.7
66.2	(400)	0.33	29.1
72.9	(331)	0.57	17.5
83.8	(422)	0.60	17.9
90.2	(333)	0.75	15.0

The observed differences in material crystallinity may be understood in the context of the Ge-X bond energies ($B.E._{Ge\text{-}X}$ [X = Cl; 390.8 ± 9.6 kJ/mol], [X = Br; 347.0 ± 8.0 kJ/mol], and [X = I; 268.0 ± 25.0 kJ/mol]).[91] While the Ge-X bond energy increases, there must be sufficient energy (*i.e.*, higher activation energy) so that the Ge-X bond will break and allow the formation of the Ge-H bond. Since higher activation energy is needed for the reaction to occur, the rate of reaction will be slower; therefore, the number of "free" Ge molecules available for reduction will be fewer. This observation leads to a slower rate of Ge reduction and a decrease in subsequent precipitation. For GeI_4, the Ge is very accessible to $LiAlH_4$ reduction; thus, the rate of reduction will be faster, and Ge(0) will precipitate quickly. If $GeCl_4$ is used instead of GeI_4, the rate of Ge reduction will be slower, and Ge(0) will precipitate slowly. The slower rate of precipitation will lead to a slower rate of nucleation, which allows better

crystals to form. Hence, increasing concentrations of crystalline Ge nanoparticles were observed in Ge nanoparticles made using a $GeCl_4$ precursor.

3.3.4. Fourier Transform Infrared Spectroscopy

FT-IR spectroscopy was used to probe particle surface chemistry. A representative FT-IR spectrum of Ge nanoparticles terminated with 1-pentene (**6a**) and hydrogen (**5b**) is shown in Figure 34; the peaks observed in the FT-IR spectra are shown in Table 9.

Prior to the hydrogermylation of Ge nanoparticles, the hydride surface is confirmed by the presence of a weak, sharp ν_{Ge-H} peak at ~ 2424 cm^{-1} to 2256 cm^{-1}.[28, 48,84] The presence of a broad peak at 3197 cm^{-1} (ν_{O-H}) on two samples (**5a** and **5b**) suggests that the surface of the Ge nanoparticle might be hydroxyl group terminated or that it is stabilized by the presence of hydrogen bond interaction between TOP and the hydride surface of the nanoparticle. The presence of ν_{Ge-O} at 879 to 910 cm^{-1} found in **5a** and **5b** suggests that hydride-terminated Ge nanoparticles can be readily oxidized.[86]

Upon hydrogermylation, the hydride surface is replaced with an alkyl chain bonded to the surface through formation of a Ge-C bond. The absence of a broad peak at 2348.97 cm^{-1} (ν_{Ge-H}) indicates that hydride termination was absent after hydrogermylation of germanium nanoparticles with 1-pentene. The aliphatic ν_{C-H} (sp^3) stretching at ~ 2956 cm^{-1} suggests that alkyl groups were present both before and after hydrogermylation. The decrease in intensity of the ν_{O-H} stretching does not rule out that hydrogen bond interactions were absent. Instead, it is unlikely that a significant degree of hydrogen bond interaction was present. The presence of significant ν_{Ge-O} at 870 to 910

cm^{-1} (present in **6b** and **6c**; absent in **6a**) implies that oxide termination was present and more energy was needed to break the Ge-O bond. Furthermore, it might also indicate that hydrogermylation was incomplete and multiple surfaces were present. The presence of $\nu_{C=C}$ at 1680 to 1600 cm^{-1} on **5a** and **6b** suggests that the FT-IR spectra confirms the presence of alkenes in the sample. The presence of the C=C stretch suggest that trace amounts of 1-pentene was embedded in the surfactant matrix.

The peaks on the IR spectra collected after hydrogermylation imply that hydrogermylation can be used to provide more uniform nanoparticle termination. The presence of multiple different peaks on the FT-IR spectra implies that the Ge surface is made up of multi-functional groups and/or hydrogermylation cannot offer 100% surface functionalization because some surfaces are not affected by hydrogermylation.

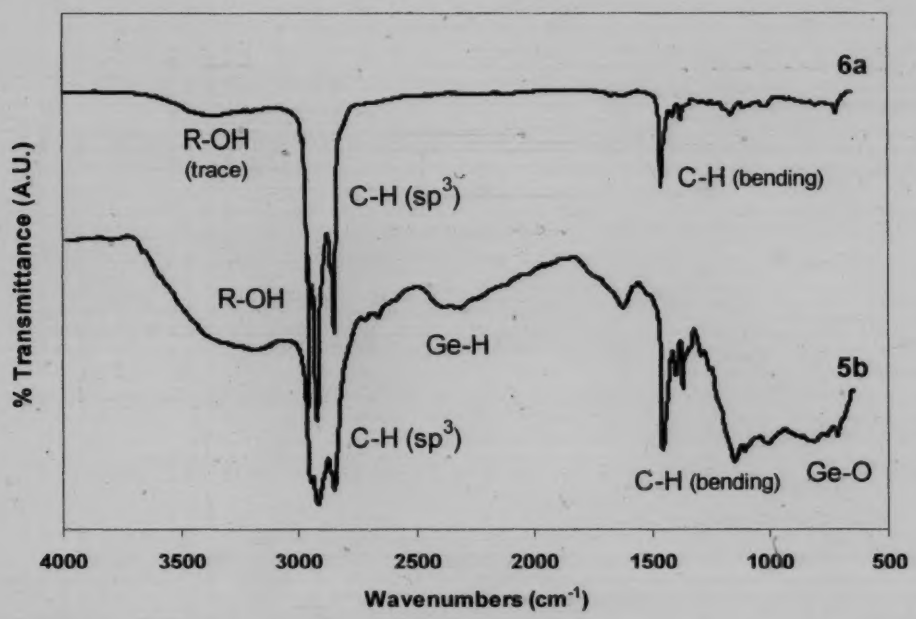

Figure 34 IR spectra of the brown products collected prior to and after hydrogermylation of Ge nanoparticles with 1-pentene.

Table 9 FT-IR data for hydride- and pentane-terminated Ge nanoparticles.

Precursor	Absorption wavenumbers (cm^{-1})
5a	3337 cm^{-1} (m, b, O-H stretching), 2916 cm^{-1} (s, s, C-H sp^3 stretching), 2413 cm^{-1} (w, b, Ge-H stretching), 1636 cm^{-1} (w, s, C=C stretching), 1429 cm^{-1} and 1370 cm^{-1} (m, s, C-H bending), 1109 cm^{-1} (s, s, P=O stretching), 897 cm^{-1} (m, s, Ge-O stretching)
5b	3189 cm^{-1} (m, b, O-H stretching), 2926 cm^{-1} (s, s, C-H sp^3 stretching), 2854 cm^{-1} (s, s, C-H sp^3 stretching), 2424 cm^{-1} (m, s, Ge-H stretching), 2361 cm^{-1} (m, s, Ge-H stretching), 1457 cm^{-1} (s, s, C-H sp^2 bending), 1405 cm^{-1} and 1194 cm^{-1} (s, s, C-H sp^3 stretching), 1012 cm^{-1} (s, s, P=O stretching), 1102 cm^{-1} (s, s, P=O stretching), 822 cm^{-1} (m, s, Ge-O stretching)
5c	2922 cm^{-1} (s, s, C-H sp^3 stretching), 2852 cm^{-1} (s, s, C-H sp^2 stretching), 2256 cm^{-1} (w, s, Ge-H stretching), 1467 cm^{-1} (s, s, C-H sp^2 bending), 1149 cm^{-1} (s, s, C-H bending), 1147 cm^{-1} (s, s, P=O stretching), 844 cm^{-1} (w, s, Ge-O stretching)
6a	2956 cm^{-1} (m, s, C-H sp^3 stretching), 2925 cm^{-1} (s, s, C-H sp^3 stretching), 2855 cm^{-1} (s, s, C-H sp^2 stretching), 1460 cm^{-1} (w, s, C-H sp^2 bending)
6b	3403 cm^{-1} (s, b, O-H stretching), 2955 cm^{-1} (s, s, C-H sp^3 stretching), 2925 cm^{-1} (s, s, C-H sp^3 stretching), 2855 cm^{-1} (s, s, C-H sp^2 stretching), 1628 cm^{-1} (w, s, C=C stretching), 1458 cm^{-1} (w, s, C-H sp^2 bending), 819 cm^{-1} (s, s, Ge-O stretching)
6c	3412 cm^{-1} (s, b, O-H stretching), 2923 cm^{-1} (s, s, C-H sp^3 stretching), 2845 cm^{-1} (s, s, C-H sp^2 stretching), 2056 cm^{-1} (s, w, Ge-H stretching), 1628 cm^{-1} (m, b, C=C stretching), 1457 cm^{-1} (m, s, C-H sp^2 bending), 819 cm^{-1} (s, s, Ge-O stretching)

3.3.5. ^{1}H Nuclear Magnetic Resonance Spectroscopy

^{1}H NMR spectroscopy provides insight into the surface chemistry of Ge nanoparticles and confirms that a hydrogermylation reaction has occurred.[31] Nanoparticles, synthesized using different Ge precursors of GeX_4 (X = Cl, Br, and I), were investigated and the NMR samples were prepared. The ^{1}H NMR spectra are used to confirm that hydrogermylation has taken place. A representative spectrum of the hydrogermylated product (**6a**) is shown in Figure 35; the related peaks are shown in Table 10.

Investigation of the ^{1}H NMR spectra shows that no alkene protons (vinyl groups) were present between 4.6 and 5.9 ppm. The presence of the vinyl group protons implies that hydrogermylation did not take place and/or terminal alkene was present in the sample. The samples were placed under vacuum for 24 hours to remove any residual alkenes and solvents. Nevertheless, residual alkyl peaks were present on two of the three spectra (**6b** and **6c**) even though the sample had been cleaned and placed under vacuum. This suggests that either the sample was not pure or more vigorous purification techniques were needed to remove any trace amounts of solvents.

The peaks on the NMR spectra of nanoparticles were also broad because of the slower rate of tumbling of the NMR timescale.[87] As the rate of tumbling decreases, the peaks on the NMR spectra broaden. While the peaks of the ^{1}H NMR spectra of Ge nanoparticles were broad, the Ge nanoparticles synthesized using $GeCl_4$ (see Figure 35) exhibit slightly sharper peaks compared with other nanoparticles synthesized using other precursors (**6b** and **6c**). The sharper peaks were more apparent in the R-CH_3 peak at 0.8 to 0.9 ppm. One can postulate that the Ge nanoparticles might be smaller in diameter; therefore, sharper peaks on the ^{1}H NMR spectra were observed because they were tumbling faster inside the NMR.[92] The TEM for Ge sample **6a** was not acquired; therefore, the diameter of the pentane-terminated Ge nanoparticles prepared using $GeCl_4$ cannot be confirmed. Based on the diameters of the hydride-terminated Ge nanoparticles prepared from different Ge precursors, one can postulate the diameter of the pentane-terminated Ge nanoparticles prepared using $GeCl_4$ would be between 1.2 and 15.1 nm. Nevertheless, the small range in diameter is not sufficient to explain why sharper peaks were observed.

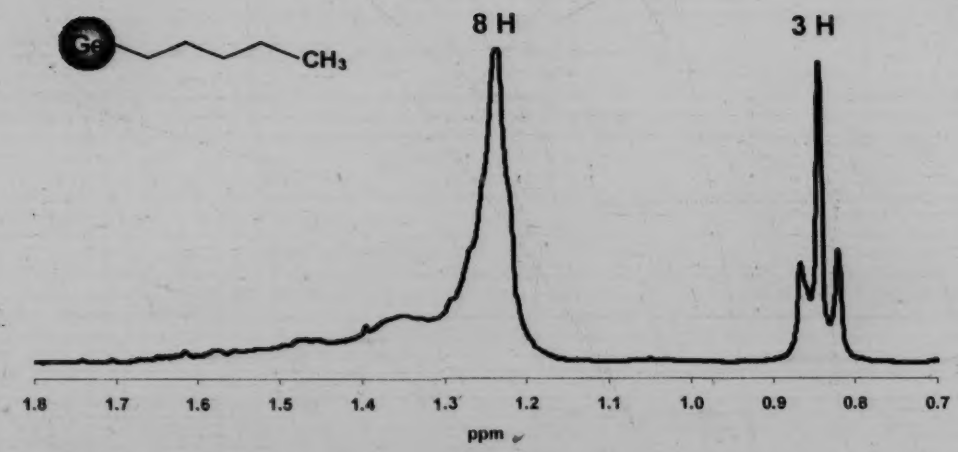

Figure 35 ^{1}H NMR spectra of the brown product synthesized using $GeCl_4$ (**6a**). This ^{1}H NMR sample was prepared using $CDCl_3$.

Table 10 ^{1}H data for alkyl-terminated Ge nanoparticles samples.

Compound	Solvent	δ (ppm)
6a	$CDCl_3$	0.844 (m, 3H, R-CH_3), 1.235 (s, 8H, R-CH_2)
6b	CD_3OD	0.903 (m, 3H, R-CH_3), 1.318 (m, 8H, R-CH_2)
6c	$CDCl_3$	0.891 (m, 3H, R-CH_3), 1.331 (m, 8H, R-CH_2)

3.4. Conclusion

An alternative method to prepare Ge nanoparticles was discussed in this chapter – high temperature (300°C) metal hydride reduction of GeX_4 (X = Cl, Br, or I). The reagents were heated to 300°C in an effort to investigate how reaction temperature influenced Ge nanoparticle crystallinity. FT-IR spectroscopy supports the presence of a hydrogen-terminated Ge surface. Transmission electron micrograph indicates the diameter of the hydride-terminated Ge nanoparticles ranged from 1.2 to 5.8 nm. The subsequent hydride-terminated Ge nanoparticles were functionalized with 1-pentene by

thermal initiated hydrogermylation. FT-IR and ^{1}H NMR spectroscopy confirms the presence of pentane in the Ge nanoparticle sample upon hydrogermylation. Transmission electron micrographs indicate the diameter of the pentane-terminated Ge nanoparticles were more polydispersed and larger (1.2 to 15.1 nm). EDX suggests that the reaction products were primary made up of Ge. X-ray powder diffraction suggests that amorphous particles were observed in hydride- and pentane-terminated Ge nanoparticles prepared using GeI_4 and $GeBr_4$. Pentane-terminated Ge nanoparticles prepared using $GeCl_4$ show amorphous characteristics; however, hydride-terminated Ge nanoparticles prepared using $GeCl_4$ show both amorphous and crystalline characteristics. The diameter of hydride-terminated Ge nanoparticles prepared using $GeCl_4$ and calculated using the Scherrer equation is estimated to range from 15 to 29 nm. In conclusion, it is shown that crystallinity of the Ge nanoparticles can be controlled by changing the halides in GeX_4.

4. Conclusion and Future Work

Solution-based approaches for the synthesis of Ge nanoparticles from the reduction of germanium halides (GeX_4) using reagents such as, lithium naphthalide (X = Cl),[32] NaK (X = Cl),[33] Mg_2Ge (X = Cl),[34] $LiAlH_4$ (X = Cl, Br, and I),[11] as well as thermally induced disproportionation of GeI_2[35] have been outlined. All known solution methods for preparing these materials suffer from significant challenges including specialized or hazardous precursors, ill-defined surface chemistry, or limited scalability. In this regard, there is a need for straightforward techniques for preparing and tailoring the surface chemistry of these materials if their full potential is to be realized.

A method of Ge nanoparticle preparation was introduced in Chapter 2. Drawing on the wide scope of literature focused on the effective synthesis of compound semiconductors via surfactant-arrested precipitation, hydride terminated Ge nanoparticles were synthesized by the reduction of GeX_4 (X = Cl, and I) using $LiAlH_4$ in the presence of a surfactant (CTAB or Triton X-100). The hydride surface termination was confirmed by the presence of ν_{Ge-H} from FT-IR spectroscopy. TEM micrographs indicate the diameter of the hydride terminated Ge nanoparticles is ca. 3 nm. The Ge nanoparticles were simultaneously purified and their surface chemistry tailored by thermally or photochemically initiated hydrogermylation with a terminal alkene. The loss of the Ge-H and appearance characteristic alkyl absorptions in the IR spectrum confirmed the Ge nanoparticle surface underwent hydrogermylation. The UV visible spectrum showed the presence of two absorptions at the direct $\Gamma_{25} - \Gamma_{15}$ transitions at Γ and X orientation; these two energy states were also found in bulk Ge. Transmission electron micrograph indicates the particle diameters of the alkyl terminated Ge nanoparticles are larger than

their hydride counterparts (*i.e.*, 2nm to 10 nm) consistent with particle growth arising from heating. The XRD of bulk Ge and SAED data confirm Ge nanoparticles possess the diamond lattice Ge structure.

In Chapter 3, an alternative method in preparing Ge nanoparticles was also investigated – high temperature (300°C) metal hydride reduction of GeX_4. Reagents were heated to 300°C in an effort to investigate how reaction temperature influenced Ge nanoparticle crystallinity. Ge nanoparticles were prepared from the reduction of GeX_4 (X = Cl, Br, I) using $LiAlH_4$ in the presence of trioctylphosphine oxide. FT-IR spectroscopy confirmed that the surface of the Ge nanoparticles was hydride terminated. TEM micrographs confirmed particle diameters ranges from 1.2 nm to 5.8 nm. The Ge nanoparticles were functionalized with 1-pentene by thermal initiated hydrogermylation. FT-IR and ^1H NMR confirmed the presence of pentyl surface termination upon hydrogermylation. Consistent with thermal functionalizations outlined in Chapter 2, TEM micrographs indicated the sizes of isolated Ge particles were more polydisperse and larger than the starting hydride terminated particles (*i.e.*, 1.2 nm to 15.1 nm). Energy dispersive x-ray analysis showed the reaction products consisted primarily of Ge. While x-ray powder diffraction showed the material crystallinity depended on the starting germanium halide. Particles prepared using $GeBr_4$ and GeI_4 are amorphous. Materials prepared using $GeCl_4$ consist of both amorphous and crystalline Ge nanoparticles. The diameter of hydride terminated Ge nanoparticle prepared using $GeCl_4$, calculated using Scherrer Equation, is estimated to range from 15 nm to 29 nm.

The present study outlines a method for preparing Ge nanoparticles from readily available precursors. In addition, the first report of tailoring Ge nanoparticle surface

chemistry via hydrogermlation was discussed. Unfortunately, the methods described suffer from many of the challenges that plague other solution-based procedures. Only small quantities of material can be prepared and with limited control over particle size. In addition, the Ge nanoparticles prepared using the presented methods exist in a surfactant matrix and reaction by-products and are difficult to purify. Using a different surfactant (*e.g.*, trioctylphosphine oxide) may partially solve the purity issues; however, this action will not eliminate the impact of reaction by-products. It is reasonable to expect that it will be necessary to use a completely different approach in the preparation of Ge nanoparticles if large quantities of tailorable materials are to be prepared. Considerations that must be considered when designing new methodologies must include easily removable byproducts, easily isolable products, and yield. One possible method may be the thermal disproportionation of germanium oxides in reducing atmospheres. Particles prepared in this way could be isolated from an oxide matrix via straightforward extraction with water and subsequently functionalized using procedures described in the preceding thesis.

5. References

1. Van Vlack, L. H. (1990). Elements of Materials Science and Engineering, 6th Edition. Ann Arbor, Michigan, Addison-Wesley Publishing.
2. Atkins, P. (1999). Physical Chemistry, 6th Edition. New York, W.H. Freeman and Company.
3. Rudden, M. N. W.; Wilson, J. (1980). Elements of Solid State Physics. New York, John Wiley & Sons.
4. Alivisatos, A. P.; *Science*, **1996**, 271, 933–937.
5. Afzall, M.; O'Brien, P.; *Journal of Materials Chemistry*, **2006**, 16, 1597–1602.
6. Derfus, A. M.; Chan, W. C. W.; Bhatia, S. N.; *Nano Letters*, **2004**, 4(1), 11–18.
7. Owens, A.; Peacock, A.; *Nuclear Instruments and Methods in Physics Research A*, **2004**, 531, 18–37.
8. Day, R. P.; Wallner, R. A.; Lodi, E. A.; *Infrared Physics*, **1961**, 212–224.
9. Gusev, K. N.; Gurov, Y. B.; Katulina, S. L.; Pavlov, V. N.; Sandukovsky, V. G.; *Instruments and Experimental Techniques*, **2007**, 50(2), 202–206.
10. Brus, L.; "Silcon Polymers and Nanocrystals," a chapter in Light Emission in Silicon: From Physics to Devices, Volume 49 in the series Semiconductors and Semimetals, Chestnut Hill, Massachusetts, Academic Press, Lockwood, D. J., Editor (1998).
11. Wilcoxon, J. P.; Provencio, P. P.; Samara, G. A.; *Physical Review B*, **2001**, 64, 035417.
12. Lu, Z. H.; Lockwood, D. J.; Baribeau, J. M.; *Nature*, **1995**, 258–260.

13. Klabunde, K. J. (2001). Nanoscale Materials in Chemistry. Manhattan, New York, John Wiley & Sons, Inc.

14. Rogach, A. L.; Talapin, D. V.; Shevchenko, E. V.; Kornowski, A.; Haase, M.; *Adv. Funct. Mater.*, **2002**, 12(10), 653–664.

15. Murray, C. B.; Noris, D. J.; Bawendi, M. G.; *J. Am. Chem. Soc.*, **1993**, 115, 8706–8715.

16. Dabbousi, B. O.; Rodriguez-Viejo, J.; Mikulec, F. V.; Heine, J. R.; Mattoussi, H.; Ober, R.; Jensen, K. F.; Bawendi, M. G.; *J. Phys. Chem. B*, **1997**, 101, 9463–9475.

17. Hua, F.; Swihart, M. T.; Ruckensteinv, E.; *Langmuir*, **2005**, 6054–6062.

18. Rowsell, B. D.; Veinot, J. G. C.; *Nanotechnology*, **2005**, 16, 732–736.

19. Zou, J.; Baldwin, R. K.; Pettigrew, K. A.; Kauzlarich, S. M.; *Nano Letters*, **2004**, 4, 1181–1186.

20. Liu, Q.; Kauzlarich, S. M.; *Mater. Sci. Eng. B*, **2002**, B96, 72–75.

21. Pettigrew, K. A.; Liu, Q.; Power, P.; Kauzlarich, S. M.; *Chem. Mater.*, **2003**, 15, 4005–4011.

22. Takagahara, T.; Takeda, K.; *Phys. Rev. B*, **1992**, 46, 15578–15581.

23. Klimov, V. I.; Schwarz, C. J.; McBranch, D. W.; White, C. W.; *Appl. Phys. Lett.*, **1998**, 73, 2603–2605.

24. Li, L.; Hu, J.; Yang, W.; Alivisatos, A. P.; *Nano Letters*, **2001**, 1(7), 349–351.

25. Manna, L.; Scher, E. C.; Li, L. S.; Alivisatos, A. P.; *J. Am. Chem. Soc.*, **2002**, 124, 7136–7145.

26. Manna, L.; Scher, E. C.; Alivisatos, A. P.; *J. Am. Chem. Soc.*, **2000**, 122, 12700–12706.

27. Rogach, A. L.; Kornowski, A.; Gao, M.; Eychmüller, A.; Weller, H.; *J. Phys. Chem. B*, **1999**, 103, 3065–3069.

28. Talapin, D. V.; Shevchenko, E. V.; Murray, C. B.; Kornowski, A.; Förster, S.; Weller, H.; *J. Am. Chem. Soc.*, **2004**, 126, 12984–12988.

29. Veinot, J. G. C.; *Chem. Commun.*, **2006**, 4160–4168.

30. Talapin, D. V.; Mekis, I.; Götzinger, S.; Kornowski, A,; Benson, O.; Weller, H.; *J. Phys. Chem. B*, **2004**, 108, 18826–18831.

31. Buriak, J. M.; *Chemical Reviews*, **2002**, 102(5), 1271–1308.

32. Kornowski, A.; Giersig, M.; Vogel, R.; Chemseddine, A.; Weller, H.; *Advanced Materials*, **1993**, 5(9), 634–636.

33. Heath, J. R.; Shiang, J. J.; Alivisatos, A. P.; *J. Chem. Phys.*, **1994**, 101, 1607–1615.

34. Tanke, R. S.; Kauzlarich, S. M.; Patten, T. E.; Pettigrew, K. A.; Murphy, D. L.; Thompson, M. E.; Lee, H. W. H.; *Chem. Mater.*, **2003**, 15, 1682–1689.

35. Lu, X.; Korgel, B. A.; Johnston, K. P.; *Chem. Mater.*, **2005**, 17, 6479–6485.

36. Gerung, H.; Bunge, S. D.; Boyle, T. J.; Brinker, C. J.; Han, S. M.; *Chem. Commun.*, **2005**, 1914.

37. Finholt, A. E.; Bond Jr., A. C.; Schlesinger, H. I.; *J. Am. Chem. Soc.*, **1947**, 69, 1199.

38. Heath, J. R.; *Science*, **1992**, 258, 1131–1133.

39. Dhas, N. A.; Raj, C. P.; Gedanken, A.; *Chem. Mater.*, **1998**, 10, 3278–3281.

40. Brus, L.; *J. Phys. Chem.*, **1994**, 98, 3575–3581.

41. Littau, K. A.; Szajowski, P. J.; Muller, A. J.; Kortan, A. R.; Brus, L. E.; *J. Phys. Chem.*, **1993**, 97, 1224–1230.

42. Bley, R. A.; Kauzlarich, S. M.; *J. Am. Chem. Soc.*, **1996**, 118, 12461–12462.

43. Mayeri, D.; Phillips, B. L.; Augustine, M. P.; Kauzlarich, S. M.; *Chem. Mater.*, **2001**, 13, 765–770.

44. Yang, C. S.; Bley, R. A.; Kauzlarich, S. M.; Lee, H. W. H.; Delgado, G. R.; *J. Am. Chem. Soc.*, **1999**, 121, 5191–5195.

45. Lee, S.; Cho, W. J.; Chin, C. S.; Han, I. H.; Choi, W. J.; Park, Y. J.; Song, J. D.; Lee, J. I.; *Jpn. J. Appl. Phys.*, **2004**, 43, L784–L786.

46. Baldwin, R. K.; Pettigrew, K. A.; Ratai, E.; Augustine, M. P.; Kauzlarich, S. M.; *Chem. Commun.*, **2002**, 1822–1823.

47. Baldwin, R. K.; Pettigrew, K. A.; Garno, J. C.; Power, P. P.; Liu, G. Y.; Kauzlarich, S. M.; *J. Am. Chem. Soc.*, **2002**, 7, 1150–1151.

48. Li, X.; He, Y.; Talukdar, S. S.; Swihart, M. T.; *Langmuir*, **2003**, 19, 8490–8496.

49. Li, X.; He, Y.; Swihart, M. T.; *Langmuir*, **2004**, 20, 4720–4727.

50. Liu, S. M.; Sato, S.; Kimura, K.; *Langmuir*, **2005**, 21, 6324–6329.

51. Tilley, R. D.; Warner, J. H.; Yamamoto, K.; Matsui, I.; Fujimori, H.; *Chem. Commun.*, **2005**, 1833–1835.

52. Booker, R. D.; Boysen, E. (2005). Nanotechnology for Dummies. Indianapolis, Indiana, Wiley Publishing, Inc.

53. Soukhanov, A. H. (1999). Encarta World English Dictionary. New York, St. Martin's Press.

54. Taniguchi, N.; *Precision Engineering*, **1994**, 16, 5–23.

55. Taniguchi, N.; *Int. J. Japan Soc. Prec. Eng.*, **1992**, 26, 1–7.

56. Eigler, D. M.; Schweizer, E. K.; *Nature*, **1990**, 344, 524–526.

57. Iijima, S.; *Nature*, **1991**, 354, 56–58.

58. Paradise, M.; Goswami, T.; *Materials and Design*, **2007**, 1477–1489.

59. Saito, S.; *Science*, **1997**, 278, 77–78.

60. Kong, J.; Franklin, N. R.; Zhou, C.; Chapline, M. G.; Peng, S.; Cho, K.; Dai, H.; *Science*, **2000**, 287, 622–625.

61. Uhlir, A.; *Bell System Technical Journal*, **1956**, 35(2), 333–347.

62. Canham, L. T.; *Appl. Phys. Lett.*, **1990**, 57, 1046–1048.

63. Bomchil, G.; Halimaoui, A.; Sagnes, I.; Badoz, P. A.; Berbezier, I.; Perret, P.; Lambert, B.; Vincent, G.; Garchery, L.; Regolini, J. L.; *Applied Surface Science*, **1993**, 65/66, 394–407.

64. Kolasinski, K. W.; *Current Opinion in Solid State and Materials Science*, **2005**, 9, 73–83.

65. Lewis, S. E.; DeBoer, J. R.; Gole, J. L.; *Sensors and Acturators B*, **2007**, 122, 20–29.

66. Gole, J. L.; Fedorov, A.; Hesketh, P.; Burda, C.; *Phys. Stat. Sol. (c)*, **2004**, S2, S188–S197.

67. Lewis, S. E.; DeBoer, J. R.; Gole, J. L.; Hesketh, P. J.; *Sensors and Acturators B*, **2005**, 110, 54–65.

68. Pingali, K. C.; Rockstraw, D. A.; Deng, S.; *Aerosol Science and Technology*, **2005**, 39, 1010–1014.

69. Jia, H.; Zeng, J.; Song, W.; An, J.; Zhao, B.; *Thin Solid Films*, **2006**, 496, 281–287.

70. Métraux, G. S.; Mirkin, C. A.; *Advanced Materials*, **2005**, 17(4), 412–415.

71. Xu, G.; Tazawa, M.; Jin, P.; Nakao, S.; *Applied Physics A*, **2005**, 80, 1535–1540.

72. Wright, J. B.; Lam, K.; Burrell, R. E.; *Am. J. Infect. Control*, **1998**, 26(6) 572–577.

73. Brus, L. E.; *Appl. Physics A*, **1991**, 53, 465.

74. Trindade, T.; O'Brien, P.; Pickett, N. L.; *Chem. Mater.*, **2001**, 13, 3843.

75. Khjairutdinov, R. F.; *Russ. Chem. Rev.*, **1998**, 67, 109.

76. Henglein, A.; *Chem. Rev.*, **1989**, 89, 1861.

77. Wang, Y.; Herron, N.; *J. Phys. Chem.*, **1991**, 95, 525.

78. Weller, H.; *Angew. Chem. Int. Ed. Engl.*, **1993**, 32, 41–53.

79. Schlamp, M.; Peng, X. G.; Alivisatos, A. P.; *J. Appl. Phys.*, **1997**, 82, 5837.

80. Klein, D. L.; Roth, R.; Lim, A. K. L.; Alivisatos, A. P.; McEuen, P. L.; *Nature*, **1997**, 389, 699.

81. Li, L. S.; Alivisatos, A. P.; *Adv. Mater.*, **2003**, 15, 408–411.

82. Huynh, W. U.; Dittmer, J. J.; Alivisatos, A. P.; *Science*, **2002**, 295, 2425.

83. Hope-Weeks, L. J.; *Chem. Commun.*, **2003**, 2980.

84. Fok, E.; Shih, M.; Meldrum, A.; Veinot, J. G. C.; *Chem. Commun.*, **2004**, 386–387.

85. Choi, H. C.; Buriak, J. M.; *Chem. Commun.*, **2000**, 1669–1670.

86. Taylor, B. R.; Fox, G. A.; Hope-Weeks, L. J.; Maxwell, R. S.; Kauzlarich, S. M.; Lee, H. W. H.; *Mater. Sci. Eng. B*, **2002**, 96, 90.

87. Hostetler, M. J.; Wingate, J. E.; Zhong, C. J.; Harris, J. E.; Vachet, R. W.; Clark, M. R.; Londono, J. D.; Green, S. J.; Stokes, J. J.; Wignall, G. D.; Glish, G. L.; Porter, M. D.; Evans, N. D.; Murray, R. W.; *Langmuir*, **1998**, 14, 17–30.

88. Gerion, D.; Zaitseva, N.; Saw, C.; Casula, M. F.; Fakra, S.; Burren, T. V.; Galli, G.; *Nano Letters*, **2004**, 4(4), 597–602.

89. Taylor, B. R.; Kauzlarich, S. M.; Delgado, G. R.; Lee, H. W. H.; *Chem. Mater.*, **1999**, 11, 2493–2500.

90. Chiu, H. W.; Chervin, C. N.; Kauzlarich, S. M.; *Chem. Mater.*, **2005**, 17, 4858–4864.

91. Lide, D. R. (2006). CRC Handbook of Chemistry and Physics. New York, Taylor & Francis Group, LLC.

92. Kim, N. Y.; Laibinis, P. E.; *J. Am. Chem. Soc.*, **1998**, 120, 4516–4517.